Functional grading of low alloy steel to 316 L by wire arc additive manufacturing – Microstructural and mechanical characterization of bi-metal interface

Galán Argumedo, J. L.; Mahmoudiniya, M.; Reinton, T. E.; Kestens, L. A.I.; Hermans, M. J.M.; Popovich, V. A.

DOI
10.1016/j.jmatprotec.2024.118305

Publication date
2024

Document Version
Final published version

Published in
Journal of Materials Processing Technology

Citation (APA)
Galán Argumedo, J. L., Mahmoudiniya, M., Reinton, T. E., Kestens, L. A. I., Hermans, M. J. M., & Popovich, V. A. (2024). Functional grading of low alloy steel to 316 L by wire arc additive manufacturing – Microstructural and mechanical characterization of bi-metal interface. *Journal of Materials Processing Technology*, *325*, Article 118305. https://doi.org/10.1016/j.jmatprotec.2024.118305

Journal of Materials Processing Tech. 325 (2024) 118305

Contents lists available at ScienceDirect

Journal of Materials Processing Tech.

journal homepage: www.elsevier.com/locate/jmatprotec

Functional grading of low alloy steel to 316 L by wire arc additive manufacturing – Microstructural and mechanical characterization of bi-metal interface

J.L. Galán Argumedo [a,*], M. Mahmoudiniya [b], T.E. Reinton [a], L.A.I. Kestens [a,b], M.J. M. Hermans [a], V.A. Popovich [a]

[a] Department of Materials Science and Engineering, Delft University of Technology, the Netherlands
[b] Department of Electromechanics, Systems and Metals, Ghent University, Ghent, Belgium

ARTICLE INFO

Keywords:
Wire arc additive manufacturing
Functionally graded material
Bi-metal interface
Microstructural characterization

ABSTRACT

This study examines the interface layer between a high-strength low-alloy steel and an overlaying austenitic stainless steel as deposited through wire arc additive manufacturing in a bi-metal block. By utilizing optical and electron microscopy techniques, and accompanied by phenomenological and thermodynamic modeling, the work elucidates on the nature of the distinct microstructural features at a new level of detail. Results showcase martensite in the form of a band along the fusion line of the first dissimilar layer, as well as in segregated islands. Within the same bead, yet away from the fusion line, an austenite matrix is identified alongside a large phase fraction of primary ferrite and sparse bainite. These findings enhance our understanding of the nature of the heterogeneous microstructure at the interface of a bi-metal build and establish empirical evidence for future modeling of microstructural development. Supplementary characterization reveals the impact of these microstructural heterogeneities on bulk mechanical performance. Hardness indents exhibit varied results along the interface, peaking at martensite islands with values up to $370HV_{0.2}$, surpassing the neighboring matrix by 50%. Under quasi-static tensile loading, bi-metallic specimens display strain partitioning along the fusion boundary, as confirmed by Digital Image Correlation. When compared to the adjoining stainless steel, the diluted interface layer exhibits superior strength (σ_y: 411 MPa) and comparable ductility (24%), leading to necking and failure away from this region. These results help predict the structural performance of bi-metal parts, and build a base for further research in more intricate loading scenarios, such as crack propagation processes.

1. Introduction

Recent growth in metal additive manufacturing has come hand in hand with a demand for large scale metallic components. Wire arc additive manufacturing (WAAM) is currently being developed as a viable option in response to such needs. This additive manufacturing (AM) method relies on the direct-energy-deposition of alloyed metal wire by means of an electric arc for the near-net shaped production of large-scale metallic components. Examples of applications range from the energy industry, where stainless steel cladding is used as a radiation resistant coating (Sun et al., 2021) to the aerospace industry, with applications such as turbine blade repair and the construction of a rocket engine end frame (Blakey-Milner et al., 2021).

As WAAM is an AM method derived from the arc welding process known and trusted by industry, it inherits important flexibilities. The WAAM method relies on the robotic control of a GMAW or GTAW welding torch. Thus, the scanning strategy and energy input may be tuned to achieve an optimal balance between process stability and microstructural control (Lin et al., 2020) in response to the geometrical constraints of each specific build. Moreover, a large variety of welding consumables is available. This enables the selection of the best alloy for each application.

The flexibilities mentioned may be exploited to produce highly optimized parts. Given that the process fundamentally allows for multiple materials to be deposited with the same AM equipment, WAAM enables functional grading of large metal parts with relative ease, often achieved in the form of bi-metal (or multi-metal) structures. This opens the door to achieve location specific properties that are tailored for

* Correspondence to: Mekelweg 2, 2628 CD Delft, the Netherlands.
E-mail address: j.l.galanargumedo@tudelft.nl (J.L. Galán Argumedo).

https://doi.org/10.1016/j.jmatprotec.2024.118305
Received 27 October 2023; Received in revised form 5 January 2024; Accepted 17 January 2024
Available online 22 January 2024

certain applications. Raut and Taiwade (2021) offer an extensive review on different bi-metallic structures available in literature, not limited to alloy combinations such as steel-nickel, steel-bronze, stainless steel-Hastelloy and many others. The possibilities for functional grading are notoriously vast, hence the importance to constrain the available options to those relevant for a given application of interest. This study concentrates on the combination of High Strength – Low Alloy (HSLA) steels with Austenitic Stainless Steel (ASS). This choice is made seeking to profit from the good ductility, fatigue, corrosion, and low-temperature performance of fcc-based stainless alloys and the superior strength and availability of HSLA steels.

The overall quality of the functionally graded bi-metal component will depend in large on the performance of the graded interface. This imposes an important problem when considering alloys that are dissimilar in nature. Problems such as solidification cracking are commonplace, such as the one presented by Sridar et al. (2022) under the context of Inconel cladding on pipe steel. Certain material combinations are susceptible to liquid-metal embrittlement, as is the case presented by Wang et al. (2023) when combining bronze and steel. A final example is offered under the context of copper and titanium dissimilar welding resulting on unwanted intermetallic CuTi phases (Mishra et al., 2023). Solutions to these problems might be as straightforward as the selection of adequate deposition parameters, or as intricate as requiring transition material, such as buttering layers. Nonetheless, available knowledge drawn from welding literature (DuPont and Kusko, 2007) shows that a defect-free joint between low-alloy steels and austenitic stainless steels is within reach, with the caveat of an often-occurring martensite phase fraction forming at the bi-metal fusion boundary. For carbon steels, post-weld heat treatment may lead to decarburization of the low alloy steel immediately adjacent to the dissimilar fusion line, leading to a detrimental effect on mechanical properties in this region (Mas et al., 2016).

Recent attempts for HSLA-ASS combinations have been carried out within the context of WAAM. Alloys ER70S-6 (HSLA steel) and ER316L (ASS) are good candidates for arc-based additive manufacturing due to their excellent weldability and availability. Under the context of single bead walls, Ahsan et al. (2019) studied the effects of dissimilar deposition of these two alloys and the microstructural development at the bi-metal fusion boundary. They found a defect-free interface populated by what is reported to be acicular ferrite, although this finding is only supported by observations done through optical microscopy. The interface is nonetheless found to respond adequately to transverse tensile testing. Further studies by the same authors (Ahsan et al., 2020) demonstrate that a post-process heat treatment can yield additional deformation capacity at the interface region, as well as strength enhancement. Additional work by Rani et al. (2022) shows similarly a defect-free interface, elucidating the differences in residual stress development for their single-bead geometry. The literature so far gives an indication of the microstructural constitution and bulk behavior of the bi-material interface layer. However, the indication of acicular ferrite is non-trivial, as the mixed chemistry is distinct from that of the surrounding material. This observation thus requires further support through detailed characterization of the microstructural constitution at the interface, including chemistry as well as phase morphology and distribution.

By committing to understand the microstructural constitution of the interface layer, the question of the geometry of the part becomes relevant. The geometry of the deposited coupon significantly influences heat dissipation during the deposition of the bi-metal part. With increasing material volume, the size of the mass acting as a heat sink grows, impacting the cooling rate. Significant evidence on the differences between multi-bead and single-bead depositions appears to lay in the microstructural development of the bi-metal interface, as observed through the presence of martensite along the fusion line. Ornath et al. (1981) attribute the martensite layer to limited liquid diffusion and negligible convection, resulting in a boundary region favoring martensite transformation. As substrate temperature increases, this boundary region expands, leading to a larger martensite band. Ahsan et al. (2020) demonstrate a clear dilution effect in single-bead WAAM, with an interface region of high hardness ranging from 300 HV to 350 HV, linked to higher Cr concentrations. Despite using lower arc power, their conditions, including high inter-pass temperature and low heat extraction capacity, foster prolonged solidification, aiding dilution, and forming a large martensite volume. Considering the apparent effect of heat accumulation in the bi-metal interface, it is concluded that depositing a thick section is advantageous for enhanced microstructural control in the bi-metal product. This higher heat extraction capacity should lead to a limited martensite phase fraction at the dissimilar fusion boundary.

Thus, the scientific gap addressed throughout this work is the need for in-depth characterization of the ferritic phases in the diluted interface layer that may lead to a mechanistic understanding of the microstructural development in the interface layer. This research gap is addressed with the methods described in the following section, encompassing the deposition of a thick-section bi-metal HSLA-ASS structure by WAAM, and the in-depth characterization of the interface layer through thermodynamic modelling, optical and electron microscopy. A deep characterization of the phases formed in the dissimilar interface is carried out, including a crystallographic analysis and transmission electron microscopy. This is done to understand the mechanisms controlling the microstructural development of the phases observed and their nature. Microstructural characterization is lastly complimented with mechanical testing, to provide a connection between the results obtained and the mechanical performance of the bi-metal part.

2. Materials and method

2.1. Wire arc additive manufacturing

The consumables selected for deposition are proprietary to the Voestalpine Boehler 3Dprint welding consumables brand ("3Dprint AM 46.", 2018; 3Dprint AM 316L.", 2019). The nominal compositions of both electrodes as stated by the manufacturer are shown in Table 2–1, and the properties at room temperature are shown in Table 2–2. These comply with the commercial specifications AWS A5.9 (AWS, 2012) ER316L and AWS A5.18 (AWS, 2005) ER70S-6. In both cases, a 1.2 mm diameter wire was used. The additive manufacturing process was carried out with a Fanuc M710iC/12 L series robot. The Cold Metal Transfer (CMT)-capable power source, wire feeder, controller and cooling unit area are proprietary Fronius systems.

A DL750 Yokogawa ScopeCorder was used to record the CMT current and voltage at a sampling frequency of 2 kHz; the consumable 3D print AM 316 L was deposited using the Fronius CMT929+P(V1.0.0.5.4) welding program, corresponding to a CMT+Pulsed deposition mode; 3D print AM 46 was deposited with a typical CMT arc mode corresponding to the Fronius CMT963(V2.3.5.2) welding program. In all cases, the welding position was perpendicular to the work piece (PA welding position). Table 2–3 shows the summary of deposition parameters, including target voltage (U) and current (I) set on the Fronius user interface, wire feed speed (WFS), travel speed (TS), contact-tip-to-workpiece distance (CTWD) and estimated heat input (HI). Heat input is evaluated as the average value over the length of any given deposited

Table 2–1
Chemical composition of wire materials as stated by manufacturer, in wt%.

	C	Si	Mn	Cr	Ni	Mo	N	Fe
3Dprint AM 46 (HSLA steel)	0.1	1.00	1.7	-	-	-	-	Bal.
3Dprint AM 316 L (ASS)	0.015	0.45	1.6	18.5	12.0	2.6	0.04	Bal.

Table 2–2
Average physical properties at room temperature of as-deposited all-weld metal per material used ("3Dprint AM 46.", 2018; "3Dprint AM 316L.", 2019). All values obtained from the manufacturer of the wire consumables except where references are indicated.

	Elastic Modulus E [GPa]	Yield Strength σ_y [MPa]	Tensile Strength σ_u [MPa]	Min. Elongation Δ/L_0 [%]	Coeff. Thermal Expansion α [μm/m/°K]
3Dprint AM 46 (HSLA steel)	209-221 (Ermakova et al., 2020)	480	580	24	13.6 (Acevedo, 2021)
3Dprint AM 316 L (ASS)	112-139 (Laghi et al., 2021)	≥ 320	≥ 510	≥ 25	16.6 (Armao et al., 2014)

bead utilizing the specification mentioned in the ISO/TR 18491 (ISO, 2015) technical report and corrected by the estimated efficiency:

$$HI = \eta \cdot \frac{U(t) \cdot I(t)}{TS} \quad (1)$$

where HI is the instantaneous heat input [J/mm], η is the process efficiency [-], U(t) is the measured instantaneous potential [V], and I(t) is the instantaneous measured current [A]. Process efficiency is assumed to be 80% (DuPont and Marder, 1995) for simplification. To shield the ASS deposit, a mixture of Ar35He2CO2 was used for the austenitic stainless steel, whilst for the high-strength low-alloy steel Ar20He12CO2 was selected. In both cases, a gas flow was set of 15 L/min.

The substrate used for welding is a commercial S690QT high-strength steel. The net shape of the coupon to be characterized is a block of 205 mm × 127 mm x 91 mm, as shown on Fig. 2–1. The first 54 mm height consist of 16 layers of 3D print AM 46. In this case, each layer consisted of 33 beads of 205 mm length and approximately 3.5 mm height. For each layer, all beads were deposited in the same direction with a 25% bead width overlap, and in the opposite orientation for the subsequent layer, as it is schematically represented in the figure. Since the start/stop regions tend to bulk-up for the given welding parameters, after the HSLA steel layers were deposited, the top beads were machined flat to begin welding the subsequent 37 mm block height of 3D print AM316L material. The effect of this procedure on the microstructural development is included in the discussion. The latter layers were completed with 26 beads per layer and 16 layers in total, averaging a total layer height of about 2 mm.

2.2. Microstructural characterization

Several techniques were used to characterize the microstructural properties of the interface region for later correlation with the mechanical properties. For Optical Microscopy, Scanning Electron Microscopy (SEM), Electron Back Scatter Diffraction (EBSD) and Transmission Electron Microscopy (TEM), specimens were extracted from the center of the block, as it is schematically represented on Fig. 2–1. To extract the specimens, the block was sectioned, mounted in conductive resin (with exception of TEM specimens), ground with SiC paper grits #80 through

Table 2–3
Wire Feed Speed (WFS), Travel Speed (TS) Contact Tip Working Distance (CTWD) Heat Input (HI), and Interpass Temperature (Int. Temp.) deposition parameters for the different wire consumables used.

	Target U [V]	Target I [A]	WFS [m/min]	TS [mm/s]	CTWD [mm]	HI [kJ/mm]	Int. Temp. [°C]
3Dprint AM 46 (HSLA steel)	21.1	143	7.5	10	17	0.27	50-120
3Dprint AM 316 L (ASS)	13.2	214	5.0	10	17	0.22	< 140

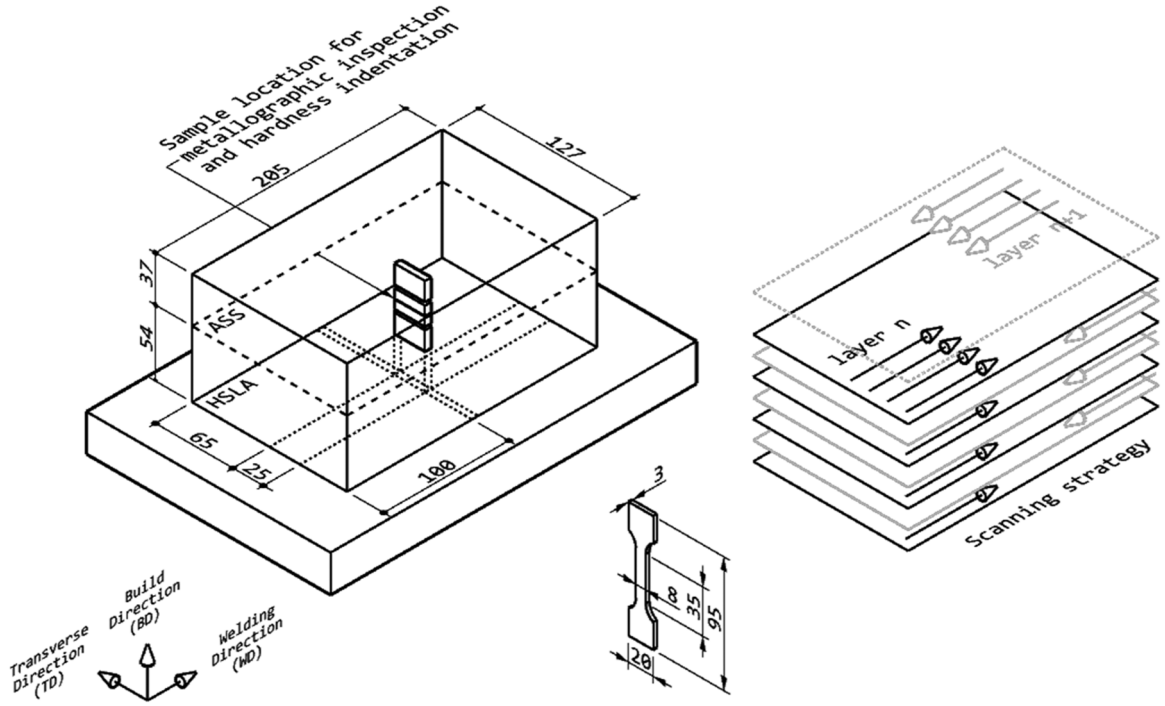

Fig. 2–1. Deposition strategy and dimensions of bi-material block, conventions on orientations and dimensions of tensile specimens. Specimen location for microstructural characterization and microhardness is indicated.

#2000, and finally polished with 3 μm and 1 μm diamond suspensions. EBSD specimens where further polished with colloidal silica suspension (OP-S) for a minimum of 45 min. Etching was done with 5% Nital to reveal microstructural features within the HSLA steel portion of each specimen; Kalling's No. 2 etchant was used to visualize interdendritic ferrite, carbides, and oxides on the ASS portion. For specimens containing the interface and the material close to its proximity, etching was carried out only for macrographic inspection following the sequence of Nital and then Kalling's No 2. This was nevertheless avoided for further microstructural characterization due to galvanic effects between both materials, leading in every case to poor delimitation of microstructural features, and partial etching at best.

Optical microscopy was carried out using a Keyence VHX-600 microscope under epi illumination. Scanning Electron Microscopy was carried out with a JEOL JSM-6500 F Field-Emission Gun Scanning Electron Microscope at an accelerating voltage of 10 kV. Backscatter Electron Imaging was used complimentarily with a Deben 5th generation 4 quadrant detector. EBSD mapping was made by a FEI® SEM-Quanta FEG 450 SEM with integrated EBSD detector. EBSD scans were carried out at a 70° tilt, 20 kV accelerating voltage. A varying step size between 70 nm for fine detail and up to 3 μm for multi-bead scans was necessary to overcome the differences in dimensional scale between features. In every case, step size is specified in each image caption, and step sizes are kept constant within the extent of each map. EBSD measurements were post-processed with EDAX-OIM Analysis™ software ver. 8.6. Stitching of large maps was performed with the aid of physical indentation marks on the specimen's surface and the stitching tools available in the mentioned software. With exception of texture analysis, a clean-up procedure consisting of a level 5 Neighbour Orientation Correlation was used with a grain tolerance angle of 5 °, restricted to clean-up points with a confidence index lower than 0.1 and a minimum grain size of 4 points. Texture analysis was done by constructing the Orientation Distribution Function (ODF) through Harmonic Series Expansion with a Series Rank (L) equal to 16 and a Gaussian Half-Width of 5 °. No symmetry (triclinic) was assumed. Parent Austenite Grain (PAG) reconstruction maps were carried out assuming a Nishiyama-Wasserman $\{111\}_{fcc}||\{110\}_{bcc}$ and $<11–2>_{fcc}||<110>_{bcc}$ orientation relationship, given the well-established fcc to bcc transformation path (Bhadeshia, 2006). For the latter analysis, an iterative orientation relationship refinement was performed, for which a tolerance angle of 5 deg. was deemed acceptable. Slight differences were observed from maps reconstructed based on Bain, Kurdjumov-Sachs and Greninger-Troiano orientation relationships; these differences are discussed briefly in the discussion Section 3.3.

Electron Probe Microanalysis (EPMA) measurements were performed with a JEOL JXA 8900 R microprobe using an electron beam with energy of 10 keV and beam current of 100 nA employing Wavelength Dispersive Spectrometry. The composition at each analysis location of the specimen was determined using the X-ray intensities of the constituent elements after background correction relative to the corresponding intensities of reference materials. The obtained intensity ratios were processed with a matrix correction program CITZAF.

Additional care was taken to prepare specimens for Transmission Electron Microscopy (TEM) characterization. Specimens of approximately 1 mm thickness were extracted with a cooled diamond cutter, and further mechanically polished to about 40 μm thickness. Disks of 2.3 mm diameter were punched out of the specimens at the bi-material interface region, glued on a 3 mm copper ring, and ion milled to electron transparency at their center. A cubed C_s image-corrected FEI Titan was used for analysis. Elemental mapping in STEM mode was done using the super-X in the ChemiSTEM ™ configuration. HREM Lattice images were collected on a Thermo Scientic Ceta ™ 16 M.

2.3. Mechanical characterization

Hardness indentations were used to obtain a measure of the local variation in mechanical properties at the interface. Vickers Hardness was measured with a load of 200 g-force and a center-to-center distance between indents and free edges of 500 μm, in agreement with minimum distance specifications by ASTM standard E92–17 (ASTM, 2017). Indentation contact was performed at a speed of 0.07 mm/s and dwell time was kept at 14 s. The indentations were performed along the build direction on the specimens used for optical microscopy.

Additionally, Digital Image Correlation (DIC) was carrier out of flat coupons loaded under quasistatic tensile testing. Six tensile specimens were extracted with the dimensions shown on Fig. 2–1. To extract the specimens, the block was sawn and the resulting slices where machined flat; water jet cutting was used to extract the final dog-bone geometry. The specimens are oriented along the build direction, across the interface layer. Single-material specimens were extracted also for the HSLA steel and ASS deposits for a comparative benchmark. During testing, a relative deformation rate of 0.005 s^{-1} was applied to the specimens at ambient temperature and humidity. The universal testing rig was controlled by crosshead displacement. Indications for zero-point setting, gripping and post-mortem calculations are done according to the ISO standard EN-ISO 6892–1:2019 (NEN-ISO, 2019). Complementary to the strain calculations, DIC was used to obtain local strain measurements in the region surrounding the bi-metal interface. The DIC system is a commercial LIMESS Q400–3D stereo camera set-up fitted with a 40 mm focal length and operating at an acquisition rate of 0.5 Hz. Speckle pattern used on the specimens was achieved with aerosol paint. The images were post-processed using LIMESS ISTRA 4D software, with which local engineering strain was estimated by a virtual gauge line of approximately 2.5 mm.

2.4. CALPHAD simulations

Thermodynamic simulations were performed with Thermo-Calc2023a. The database used for the prediction of thermodynamically stable phases included v.12. of the Steels / Fe Alloys. However, Continuous Cooling Transformation (CCT) diagrams and Scheil calculations require additional mobility data. In such cases, the v.7.0. of the Mobility database for Steel and Ferrous Alloys was used. Phases considered for CCT diagrams construction include Liquid, Ferrite, Bainite, Pearlite and Martensite. Lastly, Scheil solidification calculations were performed with the classical mode, considering carbon as a fast diffuser.

3. Results and discussion

The results and discussion section are divided in five distinct subsections to guide the reader through the intricacies of a highly heterogeneous interface layer. The description of microstructural features starts with an overview based on the observations under optical microscopy, chemical analysis, and thermodynamic modelling. As it is discussed throughout the length of these sections, the distinction of certain features is only achievable through additional supporting methods. The discussion is thus complimented by an in-depth characterization through electron microscopy-based methods. A correlation is finally established between the features observed and the performance of the interface through hardness mapping and quasi-static tensile testing.

3.1. Macroscopic inspection

Fig. 3–1 shows the macroscopic features of the interface layer, also understood as the material volume of the first ASS layer. This distinction is made from the rest of the block due to its unique microstructural features. The image is taken from a section plane normal to the welding direction. Starting with the overall geometry of the beads deposited, the distance between the two weld roots shown of the austenitic stainless steel is 5 mm. The thickness of the interface layer varies between

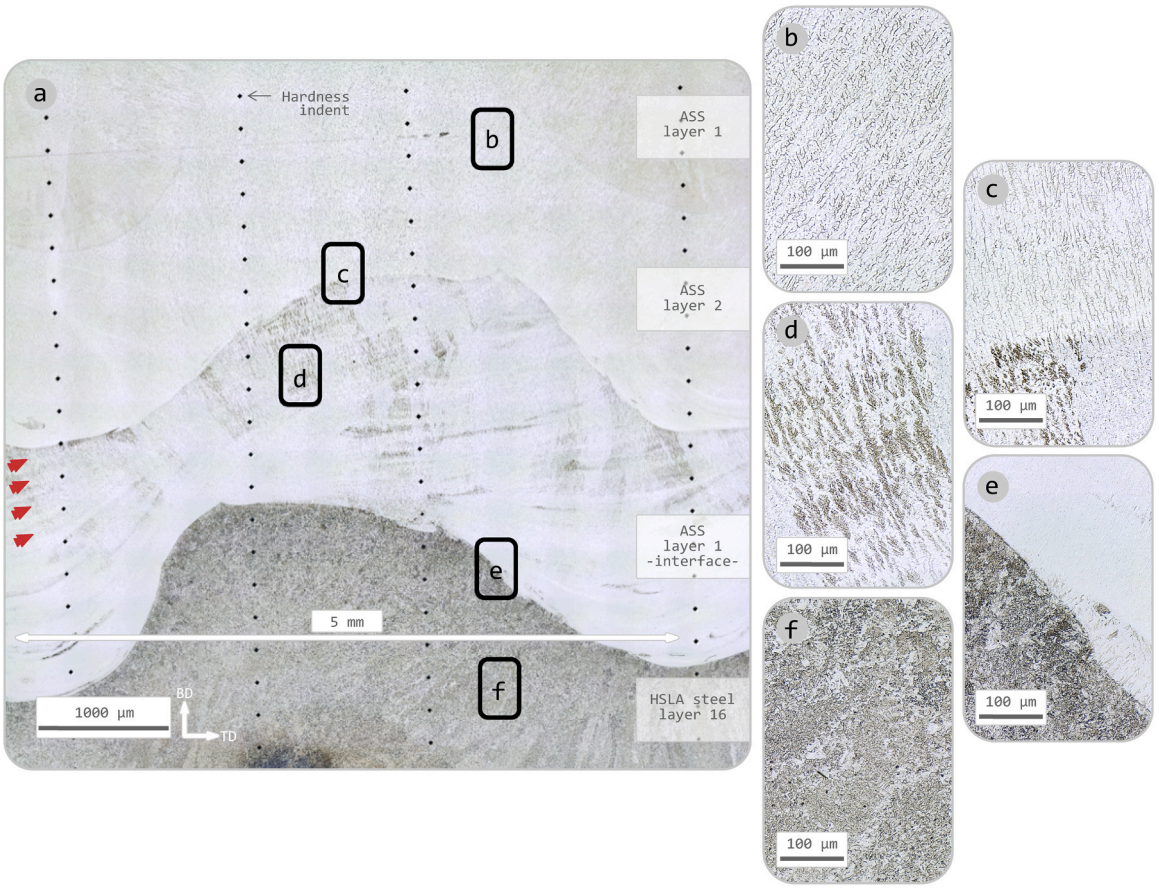

Fig. 3–1. (a) The 16th HSLA steel layer, and layers 1 through 3 of ASS, obtained with Kalling's No. 2 etchant as observed under optical microscopy including locations of hardness indents. Arrows indicate a few examples of bands formed by high amounts of ferrite. Locations of representative features under higher magnification are shown for (b) ASS matrix, (c) boundary between ASS layer 1 and 2, (d) ferritic phases within the interface layer, (e) fusion line between ASS layer 1 and HSLA steel layer 16, and (f) HSLA steel matrix.

1.1 mm on the narrowest section and extends up to 2.2 mm. Above and below the interface layer, typical microstructural features are found when considering the nature of the materials being used. On a region above the interface layer, Fig. 3–1b highlights the features typically found within an austenitic stainless steel weld deposit. The dark-etched regions show the inter-dendritic ferrite. As it has been reported in previous studies (Wang et al., 2020), the material's tendency to form large columnar grains is made evident through the parallel orientation of the primary dendrites. Opposingly, on a region below the interface layer, the HSLA steel layer 16 displays a fine microstructure of acicular ferrite surrounded by grain boundary ferrite, as it is highlighted on Fig. 3–1 f. The approximate shape and size of the Parent Austenite Grains are distinguishable through the light tonal differences, characterized by their columnar nature oriented towards each respective weld-pool center. The HSLA steel material in the immediate vicinity of the fusion line shows microstructural features typical for the Heat Affected Zone (HAZ), and are exemplified on the lower half of Fig. 3–1e. At this location, the individual Parent Austenite Grains are indistinguishable from each other. The region displays a mixture between allotriomorphic ferrite and smaller laths of acicular ferrite.

Although the bulk of the material deposited matches the microstructural development documented in previous studies (Ahsan et al., 2019; Ahsan et al., 2020), the interface layer distinguishes itself by its different microstructural development. The material belonging to the interface layer immediately adjacent to the fusion line appears un-etched on Fig. 3–1e. This effect is most likely originating from the nature of the etching process, where the low-alloy steel was preferentially attacked. Nonetheless, an area containing mostly martensite is observed. It is distinguished through mild etching of some of the martensitic lath packages.

The most distinct microstructural features are found in the middle of the interface beads, as they are shown on Fig. 3–1d. The selected etchant darkens alternating bands of a second acicular phase, undistinguishable at this magnification. These features are clustered as columnar cells and engulfed by an un-etched austenitic matrix. A detailed study of these features is presented in section 3.3. Fig. 3–1c shows the sharp boundary between the interface layer (first ASS layer) and the second ASS layer. The dark-etching features are discontinued abruptly and replaced by typical inter-dendritic ferrite. These dendrites suggest a parallel orientation relationship between the grains formed on the second ASS layer and the underlying mixed layer. The features observed in the second ASS layer are typical for additively manufactured ASS 316 L, suggesting a depreciable level of mixing for this and all layers above. This observation is further confirmed by EPMA measurements and shown on Fig. 3–2.

The unique features of the interface layer are not typical for the microstructural development of either material used. The approach to understand their distinct origin is taken through the investigation of the material's chemistry. Fig. 3–2 shows the chemical profile as obtained through EPMA analysis. There are not only evident differences in composition between the interface layer and its surroundings, but also local differences between individual features within each layer. The region left of point 1 represents the last layer of HSLA steel. Point 1 indicates the austenite matrix immediately above the fusion line, about 50 µm into the interface layer. It shows the location with highest alloying of the bead, where Cr reaches a maximum value of 18.5 wt%

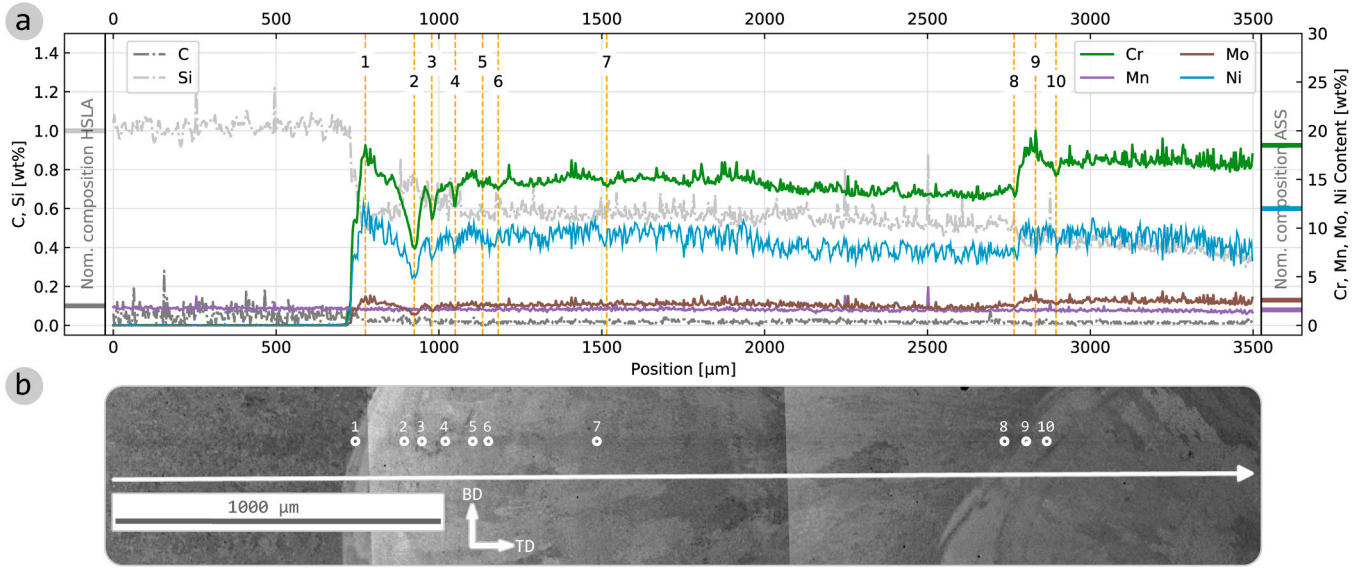

Fig. 3–2. (a) Chemical profile obtained employing Electron Probe Micro-analysis (EPMA) excluding Fe. (b) Location along which measurement was performed. Locations of interest 1 through 10 are shown. Note: measurement location was realized along the mildly visible dark horizontal band. White arrow is offset from measurement location but represents accurately length and direction of line scan.

and Ni 12.5 wt%. By contrast, point 2 gives an indication of the chemical composition of a martensite island close to the fusion boundary. At this location, a clear depletion of the major alloying components is observed, displaying Cr values as low as 7.9 wt% and Ni down to 4.9 wt%. Points 3 through 7 show locations of ferritic bands, where the difference with the rest of the material is less pronounced. Finally, points 8, 9 and 10 show the differences in chemical composition about the fusion boundary between the interface and the second ASS layer. While point 8 shows a slight depletion of Cr right below this fusion line, point 9 shows an increase in the weight fraction of alloying components, followed by a decrease at point 10 and subsequent stabilization.

A relevant phenomenon to highlight at this point is the occurrence of segregated bands across the interface layer. This is made evident through the microstructural features observed under optical microscopy in combination with the variations in chemical composition. They are indicative of segregation, whereby un-mixed or partially mixed zones form and solidify before fully mixing with the rest of the filler material. They are easily identifiable in Fig. 3–1, where some of the segregated bands are highlighted by red arrows. The heterogeneities naturally translate into scatter of the functional performance, measured through hardness in Section 3.5. Their occurrence suggests an important effect on the mechanical performance of the interface (Maurya et al., 2023). Savage, Nippes and Szekeres, (1976) gave a first indication of an 'unmixed region' between the filler material and the substrate, described solely as a zone of melted base metal. The mechanism driving this segregation away from the fusion boundary is slightly more complex. This can be attributed to a combination of convection and incomplete mixing at the fusion boundary, as demonstrated by Kou and Yang (2007) and modelled by Zhang et al. Zhang et al. (2020). in the context of dissimilar arc welding. The key criterion dictating the formation of segregated regions is a lower liquidus temperature of the weld metal compared to that of the base metal. The effect of these chemical heterogeneities on the microstructural development of the interface region are studied in further detail in the following section.

3.2. Phenomenological and thermodynamical modeling

The distinction by optical microscopy of the different phases found at the interface is not a straightforward task. Thus, additional tools are utilized, and their results are discussed. These tools include the use of empirically constructed diagrams, such as the Schaeffler Diagram, as well as thermodynamic calculations.

In Fig. 3–3, a Schaeffler diagram (Lippold and Kotecki, 2005) is presented. Through this empirical tool, it is possible to determine the effect that dilution of an austenitic stainless steel with a low alloy steel will have on the microstructural development. The three distinct features drawn on the diagram are now discussed. Firstly, the Cr and Ni equivalent values are indicated for the nominal compositions of the selected HSLA steel and ASS alloys. Under un-mixed solidification conditions, the HSLA steel alloy is predicted to solidify as ferrite and martensite, whereas the ASS is predicted to solidify primarily as austenite with about 10% volume percentage ferrite. Secondly, the effect of dilution between both alloys is approximately represented by the straight line joining the coordinates of the nominal compositions. This line crosses the regions predicting both martensite (M) and a combination of austenite and martensite (A+M). The indication of ferrite and martensite is naturally limited to the context of the Schaeffler diagram, where other occurring phases are omitted. Thirdly, the cloud of colored points represents the composition measured through EPMA at each individual position as shown on Fig. 3–3. For each position, the Cr_{eq} and

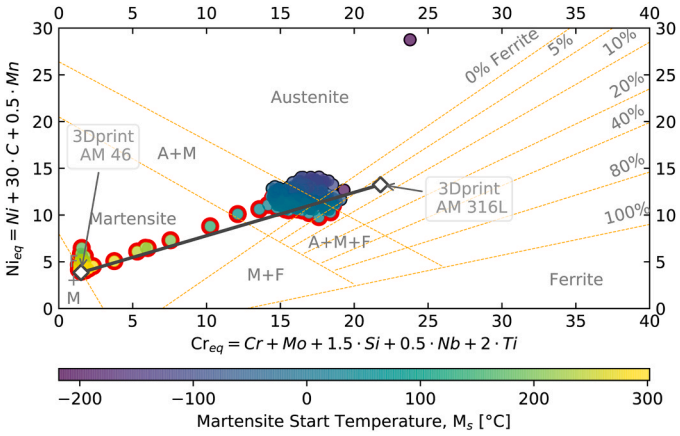

Fig. 3–3. Schaeffler diagram including Cr_{eq} and Ni_{eq} of values obtained from a line scan as measured by EPMA, see Fig. 3b. Color indicates M_s temperature. Red outlining indicates M_s temperature above 0 °C.

Ni_{eq} coordinates were calculated, and then plotted on the Schaeffler diagram. The color indicates the estimated martensite start temperature (M_s), as predicted by Self, Olson and Edwards (1984). The temperature may be determined with the color bar drawn next to the diagram. The relationship used to determine the M_s temperature is enunciated as follows:

$$M_s = 526 - 354C - 29.7Mn - 31.7Si - 12.5Cr - 17.4Ni - 20.8Mo - 1.34\cdot(Cr\cdot Ni) + 22.4\cdot(Cr + Mo)\cdot C \quad (2)$$

For ease of identification, the points that show an M_s value above 0 °C are delineated by red edges.

The Schaeffler diagram proves itself as a useful tool for the identification of the observed microstructural features. This is mostly recognized through the confirmation of martensite prediction along the diluted layer. A small variation in the Cr_{eq} and Ni_{eq} for compositions closely approximating that of the HSLA steel entails the formation of a microstructure entirely composed by martensite. These regions of limited dilution closely describe the chemistry and phase transformation occurring at the fusion boundary, as well as the segregated islands along the interface layer. The diagram does not predict the formation of

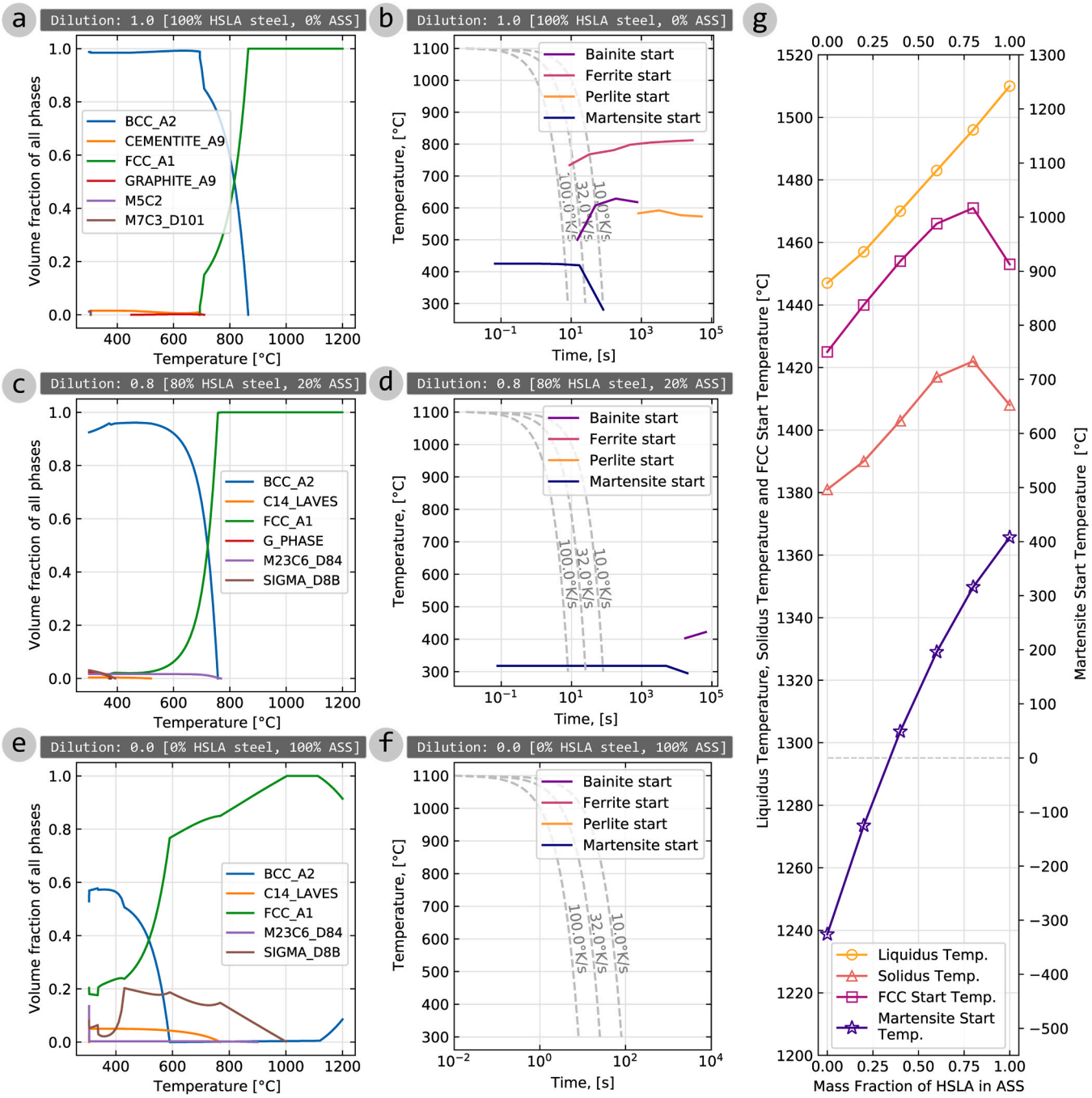

Fig. 3–4. (a) Volume fraction of all thermodynamically stable phases as a function of temperature, and (b) CCT diagram for the nominal HSLA steel alloy composition. (c) Volume fraction of all stable phases as a function of temperature, and (d) CCT diagram for an alloy consisting of 0.6 [HSLA steel]: 0.4 [ASS] (e) Volume fraction of all stable phases as a function of temperature, and (f) CCT diagram for the nominal composition of the ASS alloy. (g) Liquidus, solidus, fcc start temperature, as determined by Scheil calculations, and Martensite start temperature as a function of the degree of mixing between the nominal compositions of [HSLA steel] in [ASS]. In this case, 0.0 means a nominal composition of ASS, whereas 1.0 means a nominal composition of the HSLA steel.

bainite. This is expected, as its intended use is for high-alloy stainless steels.

Additionally supporting the findings drawn through the Schaeffler diagram, the results obtained from thermodynamic calculations are presented on Fig. 3–4. Phase volume fractions expected under thermodynamic equilibrium are shown in Fig. 3–4a, c and e for dilution levels of HSLA steel in ASS ratios equal to 1.0, 0.8 and 0.0. The selection of these specific dilution levels was done based on both nominal compositions of the alloys selected (dilution ratios 1.0 and 0.0) and a dilution level approximating the highest fcc start temperature, as shown on Fig. 3–4 g.

Fig. 3–4a shows the results obtained for the HSLA steel alloy. Firstly, above 865 °C, the only phase predicted is austenite, as it is expected for most low alloy steels. Secondly, between, 693 °C and 865 °C, the phases described under thermodynamic equilibrium include solely ferrite and austenite; these temperatures correspond to the expected A1 and A3 limits. Lastly, the plot describes a matrix composed by a large amount of ferrite, accompanied by a trace volume of pearlite for all temperatures below 693 °C. Pearlite, although not explicitly represented on the diagram, is indicated in part by the small volume fraction of cementite. The presence of pearlite, although not observed for the deposition parameters used for this study, have been reported by other authors (Huang et al., 2022). Within the same temperature range, complex carbides are also expected to precipitate, such as M_5C_2 and M_7C_3.

Studying the anticipated phases is valuable; however, it's essential to recognize that the conditions needed for thermodynamic equilibrium differ significantly from those observed during the solidification and cooling of a weld pool. Thus, a CCT diagram is presented to illustrate the solid-state phase transformations under para-equilibrium conditions. Such diagram is presented in Fig. 3–4b for the nominal composition of the HSLA steel alloy. A reasonable range of cooling rates is shown for stable arc-welding processes on the diagram, namely between 10 °C/s and 100 °C/s. Contrasting itself from thermodynamic equilibrium, the diagram predicts a lower ferrite start temperature approximating 730 °C. This same effect is also evident for the pearlite start temperature, demonstrably appearing at a temperature closer to 580 °C. Nevertheless, the most relevant difference is the indication of a bainite start temperature. As it is expected, bainite appears at higher cooling rates than pearlite. Finally, martensite start temperatures are predicted above 430 °C for the highest cooling rates, but drastically drops for the cooling rates that represent arc welding process conditions.

A mixture of 0.8 [HSLA steel] and 0.2 [ASS] naturally yields important differences in terms of thermodynamic equilibrium. This mixture is modelled on Fig. 3–4c. Pearlite is no longer predicted under this chemistry and cooling range, but the presence of additional alloying components enables the formation of intermetallic phases. Laves, sigma and the complex $M_{23}C_6$ carbide are predicted in this case. The two intermetallic phases appear at a temperature range up to 519 °C and 392 °C respectively, whereas the carbide is predicted to precipitate within a broader range, up to 768 °C. A very small volume fraction of a lesser-known G-phase is also predicted. As a short reference, the latter is formed by a stoichiometry $(Fe)_{16}(Mn)_6(Fe,Si)_7$ belonging to the cubic crystal system (Sourmail, 2001). Although the appearance of these phases could be of concern for the adequate performance of the material, their prediction is expected to be relevant only for long thermal treatments. Arguably more relevant within the context of this study is the effect of these additional alloying elements on the formation of ferrite and austenite. Naturally, the given proportion of alloying components influences the start temperature of ferrite formation. Compared to the nominal composition of HSLA steel, austenite is predicted to be stable down to 757 °C. Further cooling rapidly enables austenitic transformation to ferrite, although austenite is expected to remain within the mix of stable phases down to 371 °C.

To provide a similar comparison between thermodynamically stable and para-equilibrium conditions, a CCT diagram for the same 0.8 [HSLA steel]: 0.2 [ASS] composition ratio is presented in Fig. 3–4d. The plot distinctly lacks the indication of the ferrite start temperature, distinguishing itself from the prediction of thermodynamically stable phases. Even though bainite is predicted, this phase is not expected to be relevant for the cooling rates of interest. A bainite start temperature is foreseen only for the very slow cooling rates. The effect of additional alloying elements is thus evident. This specific composition stabilizes austenite down to 318 °C. This is also the predicted start temperature of martensite, noticeably lower than the one predicted for the nominal composition of the HSLA steel. Given that the prediction of phase transformations (or lack thereof) is accurate, it is understood that the material represented by this chemistry would appear as martensite at room temperature. This prediction extends for all mixing ratios ranging approximately between that corresponding to 0.3 [HSLA steel]: 0.7 [ASS] and up to 0.8 [HSLA steel]: 0.2 [ASS]. Within the studied cooling ranges, austenite is expected to be the only phase stable under the para-equilibrium conditions of arc welding, until the martensite start temperature is reached.

Finally, the thermodynamically stable phases of the nominal ASS alloy composition are brought into discussion. The thermodynamically stable phases and CCT diagram are shown on Fig. 3–4e and f. Within the temperature range studied, a small phase fraction of primary ferrite is expected at any temperature above 1112 °C. Down to 592 °C, most of the material is expected to remain as austenite. Below this point, only a fraction of austenite is expected to be stable throughout all cooling transformations. Precipitated ferrite is expected to be stable under thermodynamic equilibrium at temperatures below 590 °C. Also, a significant fraction of sigma and laves phases are foreseen for temperatures below 1000 °C. The appearance of both phases is strongly detrimental, even for small volume fractions. However, ferrite transformation into sigma or laves phases is only possible through an extended thermal treatment (Padilha et al., 2007), due to the sluggish kinetics (Hsieh and Wu, 2012). For the range of temperatures considered, a CCT diagram only shows a stable austenite phase, thus no boundaries are visible for the precipitation of transformation phases.

So far, the results presented do not deal with the effect of dilution on the solidification and austenite transformation temperatures. For these transformations, Scheil-Gulliver calculations are preferred. This is done to include the effects of solute re-distribution and rapid solidification. Fig. 3–4 shows the expected liquidus, solidus, austenite start temperature, as well as the martensite start temperature for all degrees of dilution. The effect of additional alloying elements in the ASS alloy becomes apparent (Pichler et al., 2020), as the liquidus line reaches below 1450 °C for the nominal composition of this alloy. Opposingly, the HSLA steel alloy shows the highest liquidus temperature, approximately 1510 °C (Soderstrom et al., 2011). Regardless of the location of the liquidus line, primary ferrite is expected to be the first phase to nucleate. However, for all dilution levels the austenite start temperature is predicted to lie between the solidus and liquidus lines. This observation indicates that regardless of the local chemical effect of partial dilution, austenite will appear before solidification is completed. Between 1.0 [HSLA steel]: 0.0 [ASS] and 0.4 [HSLA steel]: 0.6 [ASS] combination ratios, the fcc start temperature also indicates the full transformation of the readily nucleated delta ferrite into austenite. This is not the case for the rest of the compositions considered, where ferrite remains a stable phase throughout subsequent solid-state transformations as a product of segregation.

To understand the mechanisms driving solidification at the dissimilar fusion boundary, it is important to study the nucleation and initial phase transformations in detail. As it was discussed, the initial phase nucleated at 1425 °C from the liquid is a ferrite phase for the ASS. At this same temperature, the HSLA steel is transformed entirely to austenite. Assuming a situation where there is no mixing between both alloys, such conditions would lead to the conclusion that no epitaxial growth is possible as proposed by Nelson, Lippold and Mills (Nelson et al., 1999). Nevertheless, before fully solidifying, the ASS also nucleates austenite at the dendrite tips of the primary solidified ferrite (Elmer et al., 1989). The nucleation of a eutectic austenite phase is apparently true for the

mixing range between 0 and 0.8, as indicated by the Scheil-Gulliver calculations. This primary austenite phase distinguishes itself form the later occurring austenite produced through solid-state transformation of the primary ferrite while cooling. Moreover, it has been demonstrated by Inoue et al. (2000)., that for primary ferritic solidification modes, planar austenite first grows from the base metal. This phenomenon would naturally resolve the conditions necessary for the ASS weld composition to solidify under crystallographic agreement from its underlying substrate. The observations made by Inoue and Nelson are nevertheless indirect, either through crystallographic measurements or thermodynamic modelling, thus requiring further confirmation.

3.3. Microstructural characteristics of interface region

Having completed a detailed description of the chemical and thermodynamic characteristics of the interface, it is now appropriate to describe the unique features found at the bi-metal interface layer in further detail. Optical microscopy images are shown in Fig. 3–1. Nonetheless, as it was described in Section 3.1, traditional metallographic procedures lead to poor feature outlining. This effect may be attributed to the difference in galvanic properties between both alloys. Thus, back-scattered electron imaging is used to avoid any misinterpretation caused by partial etching of the two materials. Fig. 3–5a shows a low magnification image of the dissimilar interface. The features described in Section 3.1 match with those observed in this figure. Bands of a low image-quality phase, in this case assumed to be ferritic, are engulfed by a larger matrix of austenite. In the context of EBSD image quality (IQ) mapping, darker features correspond to lower IQ values. The density of features with low image quality increases at the shoulder of the bead and appears to be lowest at its root.

To gain a better understanding of the microstructural features at the interface, higher magnification images are also presented. Markers b and c in Fig. 3–5a indicate the approximate locations where Fig. 3–5b and c are located. The value of characterizing this region with backscatter electrons becomes clear, as several features can be identified. The boundary region between the last HSLA steel and the ASS layer 1 is shown in Fig. 3–5b. On the one hand, marker B highlights the location of a Type I boundary. Some small fractions of martensite form a tortuous transition between the underlying low alloy steel into the austenite matrix. From the fusion boundary, the austenite grain grows towards the center of the weld pool. Its length development is interrupted only by the martensite island highlighted by marker A. Marker C, on the other hand, shows the location of an elongated ferrite grain running parallel to the fusion boundary. Martensite is found continuously along the fusion line at this location. Across the fusion line, a grain with low IQ is observed to have developed parallel to its substrate. These features correspond with a Type II boundary. As a reference, the label Type I is assigned to those fusion boundaries where epitaxial growth proceeds from the underlying crystal substrate. From this nucleation site, growth continues perpendicular to the fusion boundary in the direction of the bead centerline. Type II boundaries, by contrast, are those where grains from the dissimilar material solidify parallel to the fusion line along the dissimilar boundary (Nelson et al., 1998).

The features observed at the boundary region do not represent those observed along the rest of the interface layer. Thus, the region away from the dissimilar fusion line is given in Fig. 3–5c in the form of an IQ map. While marker D distinguishes the austenite matrix, marker G points at the location of acicular ferrite. A few distinct lath packages may be identified, ranging between 12 to 19 μm in length and 2 to 3 μm in width at this specific location. Smaller constituents are identified alongside these lath packages, highlighted with marker F. These microconstituents are on average more equiaxed and about an order of magnitude smaller than the neighboring acicular ferrite. Marker E highlights the location of a porosity, as it becomes clear under such magnification. Due to their potentially detrimental effect on the mechanical properties of the interface, quantifying its occurrence is deemed necessary. Utilizing manual counting methods (ASTM, 2020), it is estimated that the porosity observed represents no more than 0.6% of the surface fraction, with pores not exceeding 1.5 μm in diameter.

The relationship between the different microstructural features may be best described through their crystallographic traits. Consequently, EBSD measurements were carried out across the interface layer. Fig. 3–6 presents the IPF, KAM and Phases maps of this region. As a quantitative description of the texture and phase fraction follows, it is important to indicate what is considered as the interface layer. For ease of identification, the interface layer is outlined with a dashed white line in Fig. 3–6a. The values presented in all legends belong to the entire map shown, including phase fractions and grain size distribution. By isolating the interface boundary, a 0.6 phase fraction of austenite phase is found, complimented by a 0.4 fraction of ferritic phases identified as 'iron-alpha'. Within these ferritic phases, martensite, bainite and ferrite are expected. Their spatial distribution is shown on Fig. 3–6c. Alongside the phase distribution, this figure also shows the boundaries that match the Nishiyama-Wasserman (N-W) orientation relationship within a 4° tolerance. This tolerance encompasses all Bain-like relationship, thus also possibly includes Kurdjumov-Sachs, Greninger-Toriano and Pitsch Orientation Relationships (OR) (Thome et al., 2022). These orientation relationships describe the possible orientation variations a daughter bcc

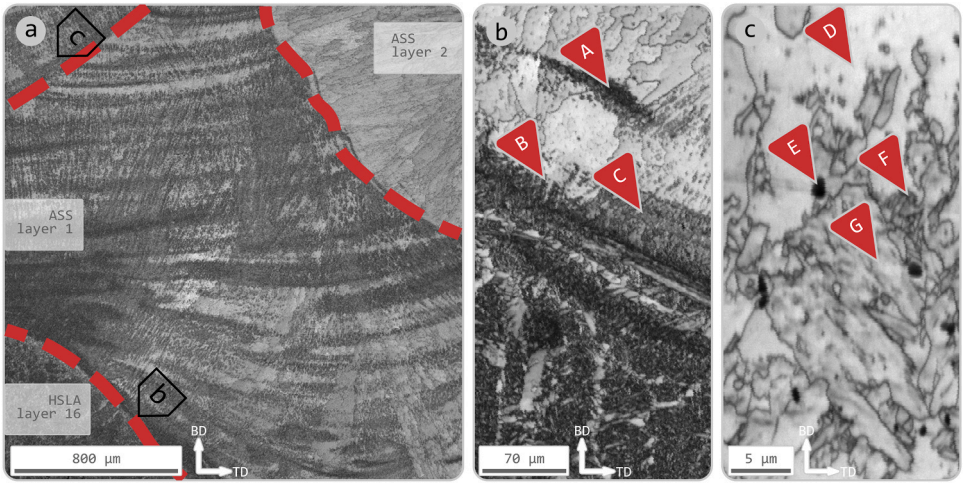

Fig. 3–5. (a) Low magnification EBSD Image Quality (IQ) map of HSLA steel layer 16, ASS layer 1 and ASS layer 2. (b) High magnification of the region around the dissimilar fusion boundary. (c) High magnification of bainitic / ferritic phase within the ASS layer 1 and away from the dissimilar fusion boundary.

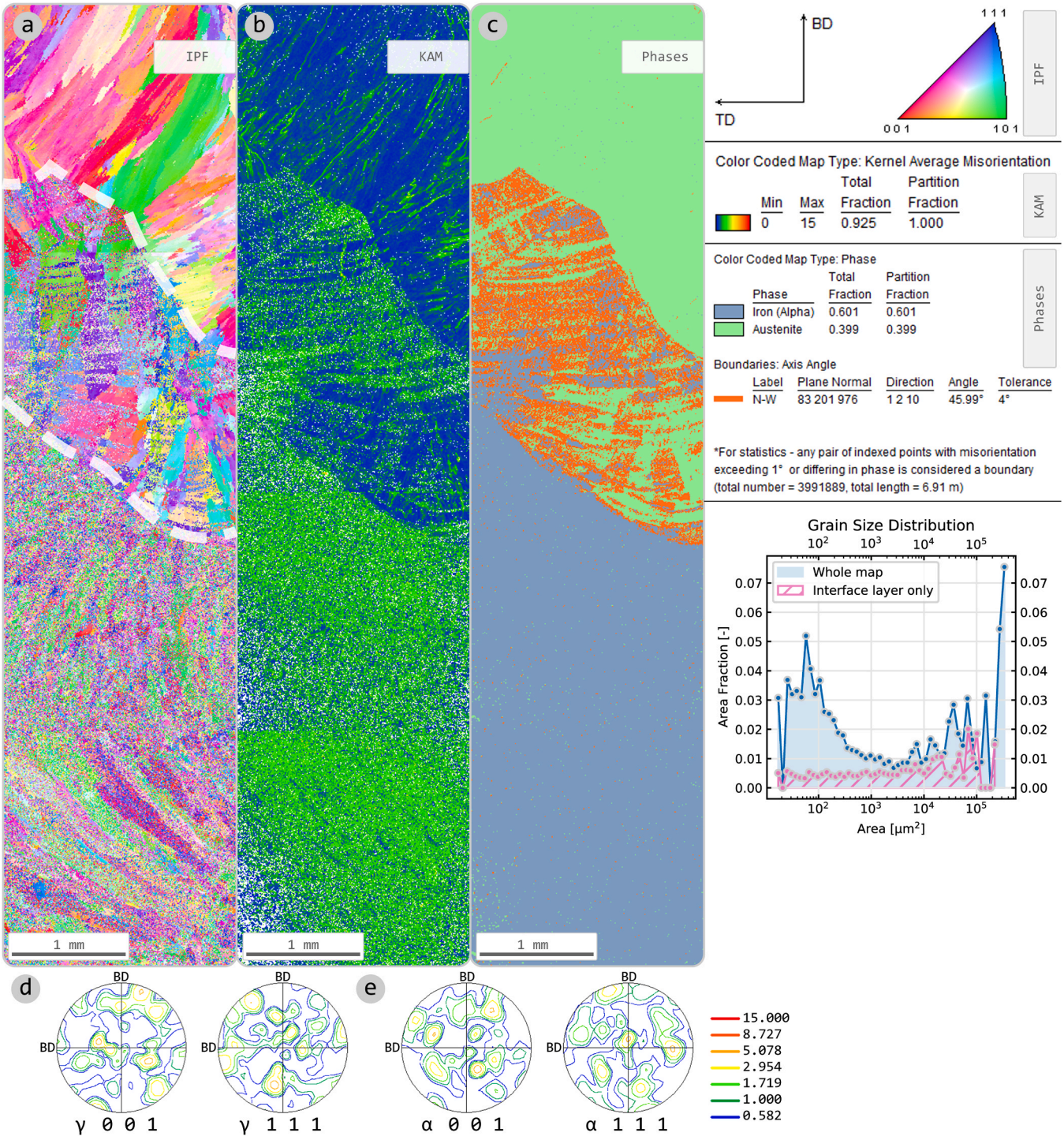

Fig. 3–6. (a) Inverse Pole Figure (IPF) mapping of multiple beads around the dissimilar interface obtained with a step size of 3000 nm. (b) Kernel Average Misorientation (KAM). (c) Phases map, where white pixels represent points indexed with a confidence interval lower than 0.1. Pole figures showing stereographic representation of ODF as measured at the interface layer are provided for (d) the fcc phase and (e) the bcc phase. Pole figures are obtained from the region delimited by white dashed line on figure a. Legend includes reference axis to maps, IPF, KAM, Phase map color legend, and grain size as a function of area fraction for the entire map shown.

phase may display with respect to the parent fcc phase. As it is clear from this map, all ferrite-austenite boundaries comply with this criterion.

The maps shown on Fig. 3–6a gives an indication of the crystal orientations, grain shapes, and sizes within and around the interface. The IPF map is obtained with respect to the build direction (BD) to easily identify texture components along this direction. Columnar grain development is clear, even across the ferritic constituents found all throughout the layer. As it has been identified that the orientation of the ferritic phase within any given austenite grain is coherent (Bain-like), all ferrite features within the same grain appear to have the same inverse pole orientation. Nonetheless, a preferential crystallographic orientation of $< 001 >$ aligned with the build direction is not recognizable, although it is typical for fcc materials in the context of AM. KAM mapping accentuates the differences between the austenitic and ferritic

phases, even as intertwined as they appear within the dissimilar interface. Grain Average KAM values (also known as 'AMIS' (Githinji et al., 2013)) for ferritic phases included exclusively within the interface layer display an average value of 1.62°. Opposingly, the austenite fraction displays a value of 1.04° under the same metric. This may be qualitatively confirmed through the color mapping shown in Fig. 3–6b.

Although low magnification maps reveal useful information about the interface layer, the dissimilar boundary is best studied locally under higher magnification in Fig. 3–7. Thus, the description of the crystallographic features continues with a detailed analysis of the HSLA-ASS dissimilar fusion boundary. In Section 3.4, this characterization is complimented with Transmission Electron Microscopy. These results are useful to elucidate the nature of all the phases identified as bcc, given that the distinction between martensite, bainite and acicular ferrite is non-trivial. The location mapped coincides with the one shown on Fig. 3–5b. As the identification of specific features may be troublesome within the map, labels are provided for the identification of Type I and Type II boundaries, as well as the outlining of the corresponding crystals.

For the region identified as Type I boundary, two relevant features are identified. Firstly, martensitic packages are observed populating the fusion line. These packages are shown closely oriented to $< 100 >$ on the IPF map in Fig. 3–7a. They are distinguished being martensite due to their high misorientation values. The martensite laths show a 1.47° grain average kernel misorientation and grow up to 15 μm beyond the fusion line. As a comparative reference, the austenite crystal immediately adjacent shows a value of 0.52°. The second feature of interest is the OR between the martensite phase and the austenite crystal. As it is shown on Fig. 3–7c, the N-W OR shown in orange describes accurately the boundary between both phases within a 4° tolerance. This is true not only for the martensite found at the fusion line, but also for the martensite island found detached from said region. Parent Austenite Grain reconstruction further clarifies the origin of this observed orientation relationship. Both the martensite found at the fusion line and the one found in the detached island have originated from the same parent grain. Moreover, the ferritic phases immediately below the fusion boundary show a coherent PAG orientation with respect to the austenite crystal. This result reveals crystallographic agreement and growth of the austenite grain across the fusion boundary.

The boundary region identified as Type II distinguishes itself from the Type I boundary through a few key features. Alongside the dissimilar boundary, a ferritic grain is observed. This grain is nevertheless not homogeneous, as it is populated with smaller features. Along the fusion line, lath martensite is found oriented towards the center of the weld bead, alongside few isolated inclusions of retained austenite. The remaining features within the ferritic grain display a high value of KAM, where the observed value of grain average misorientation is estimated to be 0.82°. Nonetheless, the Image Quality is higher than the austenite matrix, yet not as high as that of martensite. It is important to point out that Image Quality is a measure of the relative quality of the Kikuchi patterns, which in part vary due to microstructural imperfections. This observation suggests that the nature of the ferritic phase is either idiomorphic ferrite or bainite if compared with the observations made by Baek et al. (2020). PAG reconstruction indicates that the ferritic and martensitic constituents may have originated from the same parent

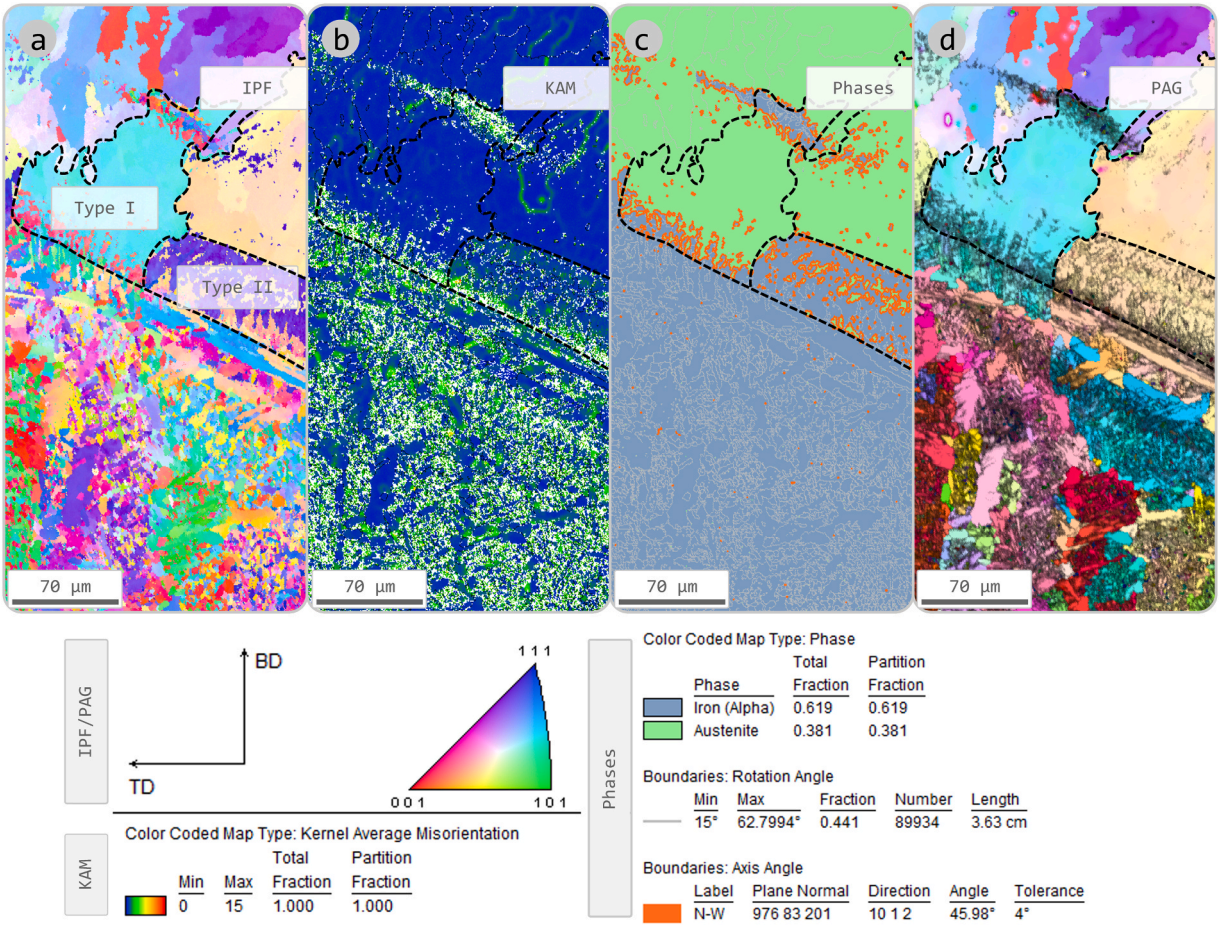

Fig. 3–7. (a) Inverse Pole Figure (IPF) of boundary region between last layer of HSLA steel and the interface layer, obtained with a step size of 700 nm. (b) Kernel Average Misorientation (KAM). (c) Phase map showing grain boundaries larger than 15° in white and boundaries that match the N-W orientation relationship. (d) Parent austenite grain reconstruction overlayed on the Image Quality map. Legend includes reference axis to maps, IPF, KAM, Phase map color legends and large angle grain boundary length.

grain, which only partially transformed to the grain observed at room temperature. The austenite retained within the grain matches the orientation of the parent grain. This reconstruction map thus reveals that such grain and all its internal features may come in crystallographic agreement with its prior-austenite substrate and partially transformed to three different phases.

The existence of a Type I boundary alongside a Type II boundary is an observation that demands further discussion. The Type I boundary follows the conventional austenite-ferrite dissimilar fusion boundary, as presented by Ornath et al. (1981). Due to the friction between the liquid and the solid phase, fluid flow is reduced at the weld pool boundary (Kou, 2021). Thus, a small material volume of scarcely mixed base metal can still exist. Under the condition of limited mixing, the chemical composition favors the formation of martensite, as it has been demonstrated and discussed in Section 3.2. This same mechanism leading to limited mixing at the fusion boundary may also promote the reduction of the solidification temperature, at an intermediate temperature between that of the base material and that of the layer being deposited. Thus, this scarcely mixed region may re-solidify before the rest of the weld-pool.

Kou and Yang (2007) further extended this macro-segregation mechanism by indicating the effect of convection within the weld pool. Their work indicates that the partially mixed volume fraction could be lifted behind the weld pool, forming either peninsulas or islands. A peninsula is understood as a volume of unmixed (or scarcely mixed) base material that is lifted through convection but remains in continuous contact with the fusion boundary. An island, by distinction, refers to that material volume that completely detaches from the fusion boundary and yet retains a scarcely mixed composition. This convection mechanism may thus give an explanation between the different boundary types observed alongside the fusion boundary.

Continuing with the description of the unique features within the interface, the crystallographic description of the region captured in Fig. 3–5c are illustrated on Fig. 3–8. The IPF map on Fig. 3–8a gives a clear indication of the closely matching orientations of the major laths observed. This observation confirms that the feature observed is indeed a single lath package. The acicular microconstituents, nonetheless, display high angle boundaries when compared to the bainitic laths. The high angle boundaries are found to match a rotation angle close to either 52° or 59°, falling within the most typical ranges of acicular ferrite (Shrestha et al., 2014). Low angle boundaries help distinguish the different lath packages within the feature. Point-to-origin misorientation mapping across one of the larger laths reveals that it is made up by 4 distinct packages of approximately 1.5 μm in width. These packages are in turn divided by a boundary misorientation between 0.5 to 3°. Kernel Average misorientation mapped in Fig. 3–8b shows a very low density of relevant features at this magnification. Even so, the grain average misorientation highlights the differences for all three constituents present. While the austenite matrix displays a value of 0.27°, the large bainite laths show a grain average misorientation of 0.52°. Notwithstanding the largest value observed, the neighboring microconstituents reach an average value of 1.1°. Alongside the IPF and KAM maps, the reader is provided with the phase map in Fig. 3–8c. This includes high angle boundaries drawn for ease of identification of the microconstituents. The boundaries matching the axis-angle criterion of N-W OR are highlighted in orange. These boundaries illustrate the Bain-like relationship between fcc-bcc phase constituents belonging to the same parent grain, including those of bainitic nature.

The possible identification of acicular ferrite within the interface

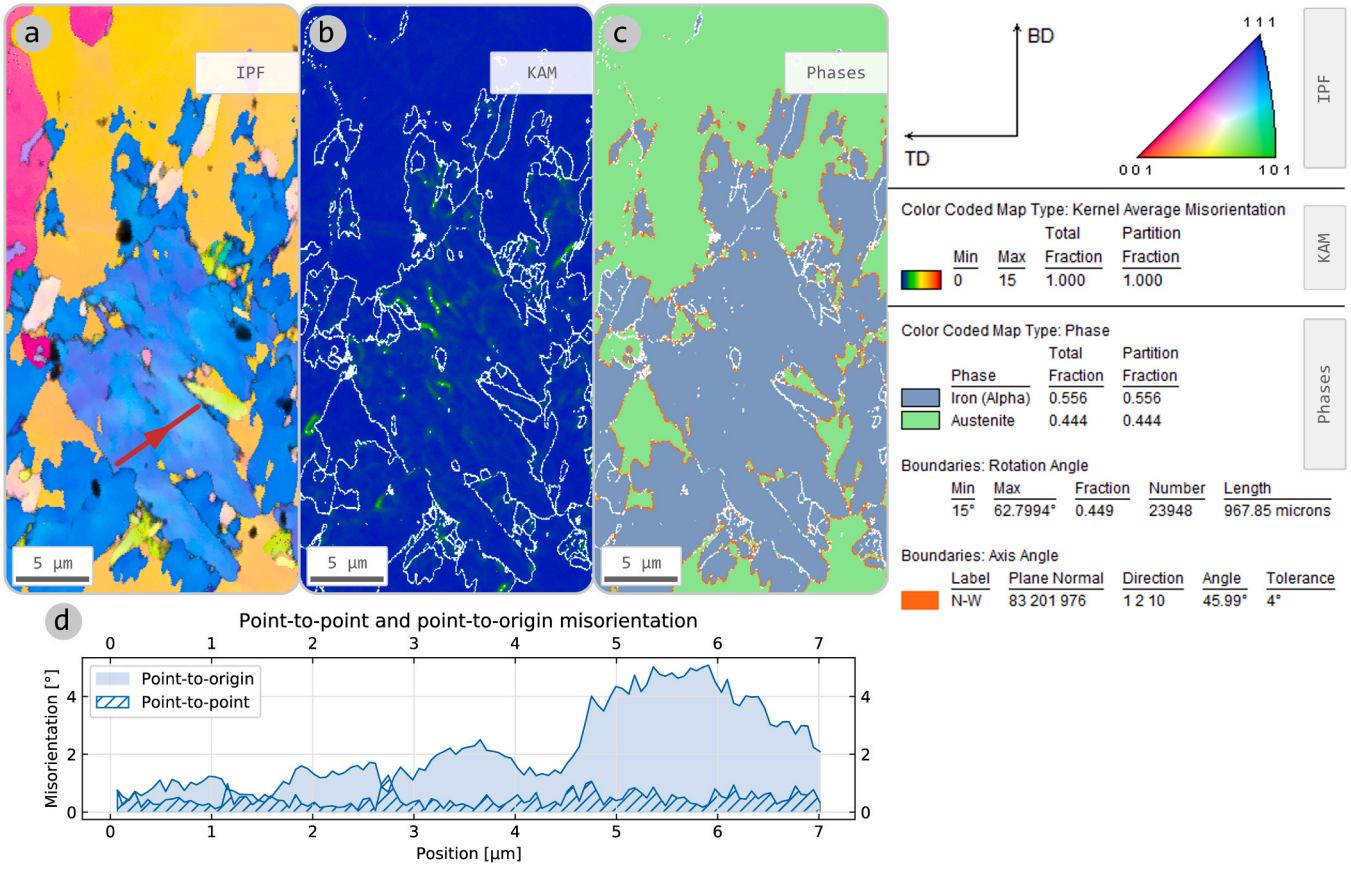

Fig. 3–8. (a) Inverse Pole Figure (IPF) of bainitic island within interface layer obtained with a step size of 70 nm. (b) Kernel Average Misorientation (KAM) showing grain boundaries larger than 15° in white. (c) Phase map highlighting boundaries that match with N-W orientation relationship. (d) Point-to-point and point-to-origin misorientation profile at location marked in (a). The legend includes reference axis to maps, IPF, KAM and Phase map color legends, as well as total grain length density of boundaries matching the orientations of interest.

layer delineates the degree at which segregation might occur. Para-equilibrium calculations discussed in Section 3.2 indicate the range at which bainitic transformation is expected. Departing from the nominal composition of the HSLA steel filler wire, any mixing larger than 10% of the ASS into the HSLA steel composition leads to sufficient austenite stabilization to overcome any transformation other than martensite. The orientation relationship between the ferritic phase and the austenite matrix matches throughout its entire periphery by a Bain-like rotation. This naturally indicates the precipitation of this ferritic phase from the parent austenite grain. The ferrite constituents contained within the same austenite grain share the same crystallographic orientation as the ferritic phase shown in Fig. 3–8. The lack of martensite laths in its vicinity suggests the lack of a mixed alloy composition described in previous sections. Thus, an alternative mechanism must be controlling the solid-state phase transformations. For this, TEM characterization is carried out to confirm the description of phases observed.

3.4. TEM characterization

As it has been shown throughout the methods employed up to this point, the interface layer presents a large variety of phases of different morphologies. These may range from the austenite matrix to a mix of ferrite constituents, including products of the partial solid-state transformations of the stainless steel, bainite, allotriomorphic ferrite, idiomorphic ferrite as well as martensite. Most of these phases are identifiable through the distinction of their etching, through their crystal characteristics, or through traits shown by a combination of methods. Nevertheless, acicular ferrite, also understood as intragranular bainite (Rees and H.K.D.H, 1994), and martensite both form laths and packages that could easily be mis-identified through either method. The most adequate way to confirm the presence of both phases is thus through Transmission-Electron Microscopy (TEM). TEM analysis is also used to confirm the size and frequency of occurrence of important nanostructures relevant for the adequate mechanical properties of the alloy, such as dislocation structures and small precipitates.

As a first step, the features typical for the austenite matrix within the interface layer are introduced. Fig. 3–9a shows a location alongside the foil edge including two different grains separated by a low angle boundary. A high-density network of tangled dislocations is immediately recognizable. The average size of these cells is estimated to lie between 0.41 and 0.54 μm in diameter. Dislocation cell walls are observed to occur independent of any spatial chemical segregation.

An important effect yet to be understood is the development of a higher dislocation density when carrying out depositions of thick sections. Bertsch et al. (2020) derived this conclusion from a systematic study on thermomechanical constraints during Laser Engineered Net Shaping, a form of Direct Energy Deposition. This dislocation development has a direct consequence on the material's mechanical performance, as it has been established that dislocation pile-ups moderate the twinning of austenite (Liu et al., 2018). The authors state that this mechanism improves the yield behavior of the alloy without compromising its ductility. Nonetheless, the pileups observed are not spatially correlated neither with the dendrite structures nor with any elemental segregation like those observed by Bertsch et al. (2020), leading to an un-organized cell structure. This important difference can be attributed to the slower cooling rates of WAAM compared to LENS (Izadi et al., 2020), resulting in a different solidification mode and also a less dense dislocation build-up.

Additional features may be observed under even further magnification. Appearing within the austenite matrix, high resolution imaging reveals a high density of planar dislocation arrays. These features are pointed by markers on Fig. 3–9b, and have been correlated with the accommodation of small plastic strain (Bayerlein et al., 1989). As the density of stacking faults is closely related to the composition of the alloy (Lu et al., 2016), it is important to note that their density will vary along the variations of chemistry across the interface layer. The largest density of stacking faults is thus expected in the regions of highest Ni and Mn concentration (Lu et al., 2016). Moreover, stacking faults will aggregate in the close vicinity of precipitates with a mis-matching lattice, such as the oxides found in the austenite matrix.

Some phases and particles typically present in the volume fraction of the ASS are found alongside the fcc matrix within the interface layer. A feature that has not been highlighted so far is the interdendritic ferrite. An example of this phase constituent is shown in Fig. 3–10a. EDS line scanning in Fig. 3–10b reveals the well-known segregation of Cr into the interdendritic spaces during solidification. Features both within the interdendritic ferrite and the austenite matrix are visible, highlighting thus their close orientation relationship. The zone axis matches bcc [110] for this image, clearly highlighting the high dislocation density found within this ferritic phase. Alongside the ferrite constituents, Si-Mn oxides are found. The oxides are located both in the austenite matrix and along the ferrite precipitate. The composition of these particles is identified through the EDS elemental maps provided in Fig. 3–11. Their size is estimated between 0.15 and 0.25 μm in diameter, and the distance to the nearest neighbor particle observed ranges between 0.85 and 1.4 μm.

The last features to be described are those of acicular nature, exemplified by those features seen in Fig. 3–5c and again in Fig. 3–8. Under TEM imaging, bainite laths are easily identifiable. An example of these bainite laths is shown on Fig. 3–12a, where 8 plates are visible and numbered. The plates are contoured by the austenite film which matches in crystallographic orientation with the rest of the matrix observed. The

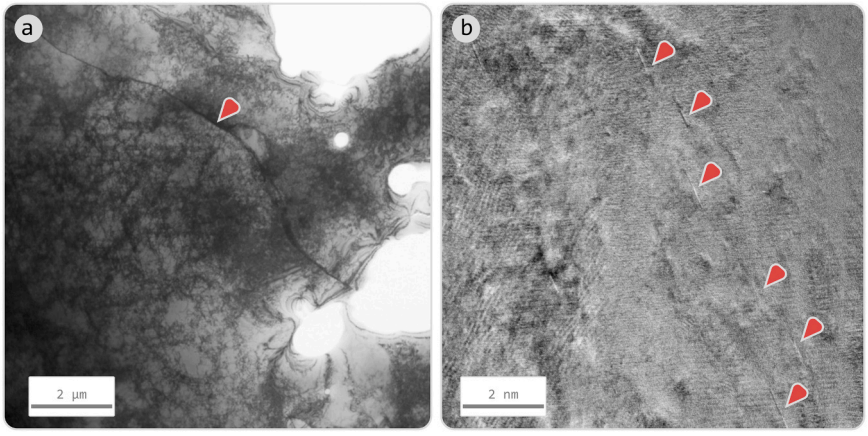

Fig. 3–9. (a) Transmission Electron Microscope (TEM) Bright Field (BF) image of austenite matrix including a low angle grain boundary. (b) High-Resolution TEM (HREM) image showing a group of planar dislocation arrays in the austenite matrix.

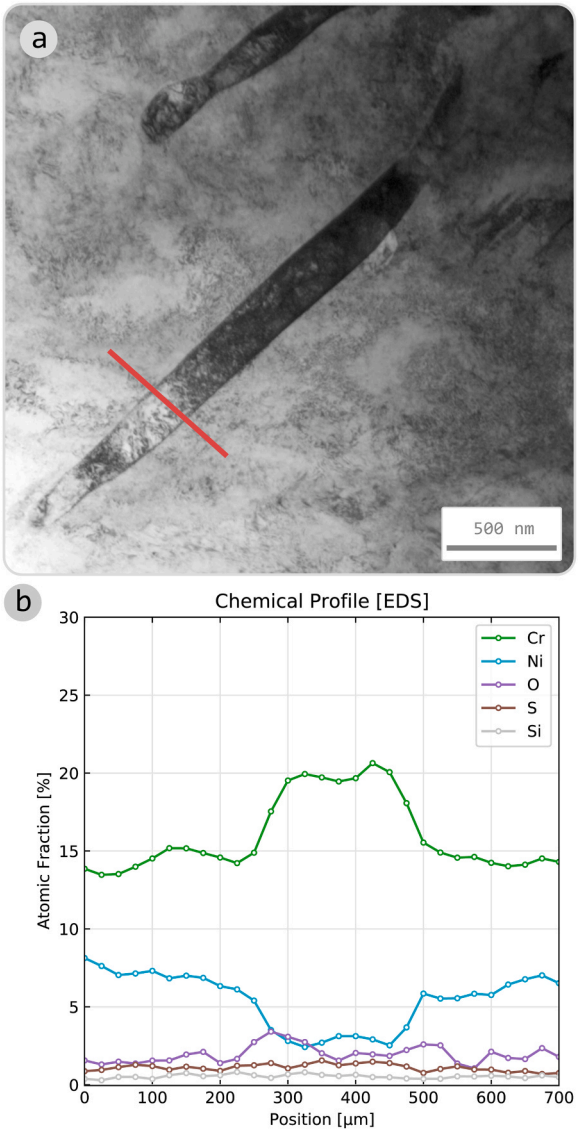

Fig. 3–10. (a) TEM-BF image showing interdendritic bcc phase entirely contained within an fcc matrix indicating the location of the EDS chemical profile shown in (b).

austenite film between them appears dark, as it originates from a dislocation cell wall. The plates display an average thickness of 0.09 µm, and the whole lath has a total width of 0.97 µm. Contrastingly, lenticular plates are shown crossing a location of high dislocation density in Fig. 3–12b. These features are much longer and thinner, possibly indicating the location of lenticular martensite. The plate thickness varies from 10 up to 80 nm. The dislocation density found within the lenticular plates is negligible when compared with the austenite matrix within which it is found. This observation serves as an indication of the possible driving mechanisms leading to the formation of this phase. The fcc austenite matrix, a bcc phase and a fraction of a lenticular plate are shown near each other in Fig. 3–13. The twin nature of the lenticular plate is made evident under this high-resolution image shown in Fig. 3–13b. The orientation relationship between the bcc and the fcc phases is illustrated through the FTT transformation of the image, which in turn simulates the selected area diffraction pattern of both crystal lattices. Under the 100_{bcc} // 011_{fcc} zone axis, a corresponding orientation relationship is apparent between both phases.

3.5. Mechanical performance

As an indirect measure of local mechanical performance, Vicker's hardness measurements were carried out. Their locations are shown on Fig. 3–1a. The interface shows microstructural features which are discontinuous. This includes Type I and type II boundaries, as well as occasional martensite islands within the austenite matrix. To overcome this problem, the hardness values were obtained at several locations along the dissimilar interface, noting their relative distance from the dissimilar fusion line. These results are presented graphically on Fig. 3–14. The aggregation of results in a single error bar plot highlights the variation in hardness in the proximity of the fusion boundary. The highest value observed is measured within a martensite island 250 µm away from the fusion boundary, reading a value of 371 $HV_{0.2}$. Nonetheless, without the presence of a hard face like martensite, indents at the same location yield a hardness of 220 $HV_{0.2}$. The highest variability is observed between 750 µm below the interface and 1250 µm above it. This region corresponds to the coarse-grained HAZ of the last HSLA steel layer, the fusion boundary, and the lower half of the interface layer. Although martensite was observed at the fusion boundary, the largest variability arises from the detached martensite islands.

The differences in hardness observed through the interface only give a first indication of its mechanical behavior. Tensile tests are thus conducted to understand the deformation behavior of the bi-metal component under tensile loading. To overcome the limitations posed by the relative size of the region of interest, DIC is used to monitor the deformation of the diluted interface. Fig. 3–15a shows the load-deformation curves of the 6 tensile specimens examined in this work. The apparent low stiffness shown in the curves is expected since the displacement measurements are taken from the crosshead of the testing rig. Nonetheless, an important phenomenon is highlighted in the zoom-in insert included in the figure. After a gradual deviation from linear-elastic behavior through relaxation, all specimens show a slight and sudden increase in stiffness at about 8.5 kN. This inflection point is then followed by substantial work hardening up to the maximum tensile

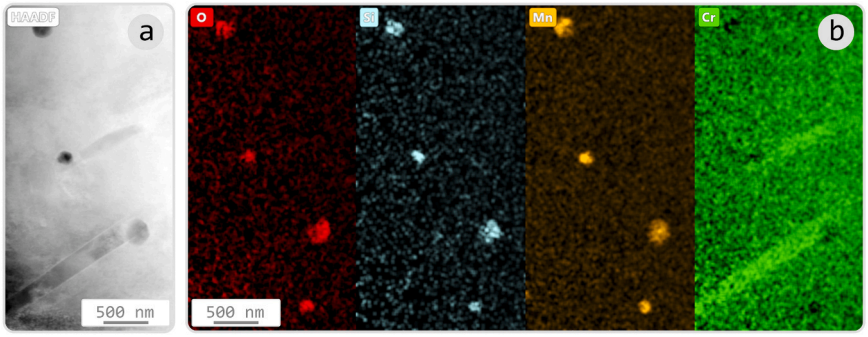

Fig. 3–11. (a) High-Angle Annular Dark Field Imaging (HAADF) showing (b) the compositional maps of the same region including from left to right oxygen, silicone, manganese, and chromium. These images are obtained at the same location as Fig. 3–10 in the interface layer.

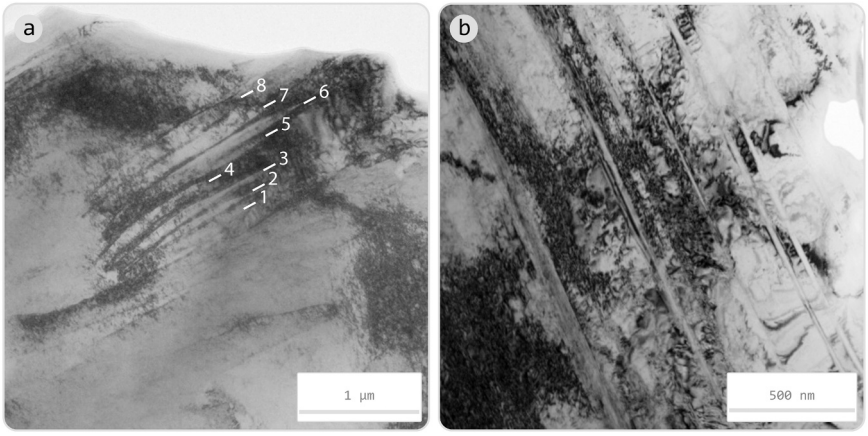

Fig. 3–12. (a) TEM-BF image showing lath-like cells enclosed alongside dense dislocation clusters. (b) TEM-BF image showing an alternative example of lamella twins within the austenite matrix at a different location.

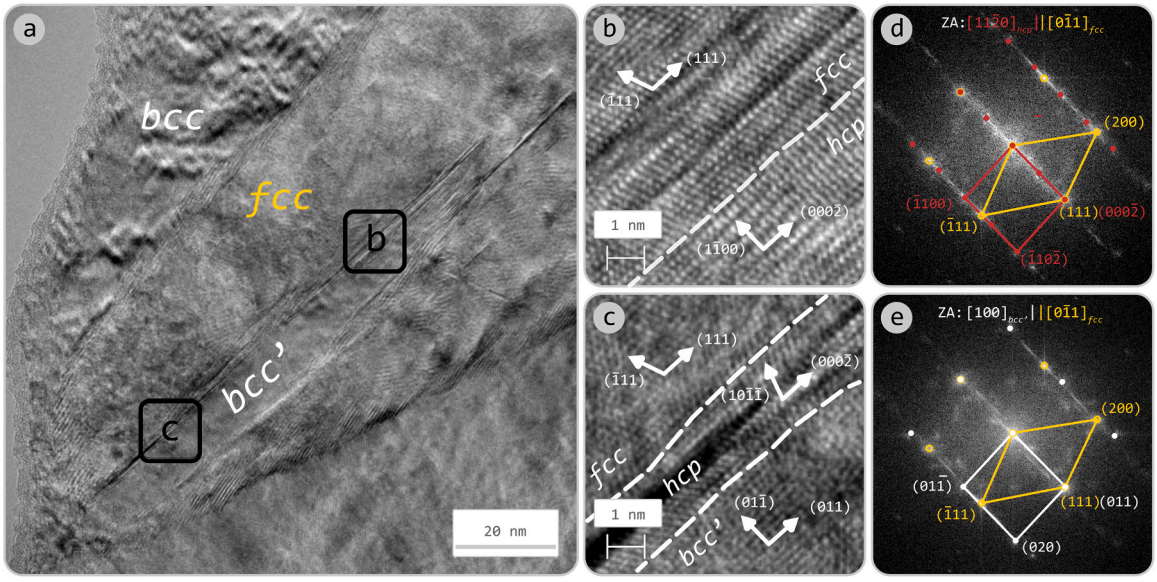

Fig. 3–13. (a) HREM of bcc phases surrounding the austenite phase with a martensite plate originating from its grain boundary, Zone Axis [001] bcc || [011] fcc. (b) Higher magnification region including HCP martensite (c) Higher magnification region including bcc martensite, hcp transition region and fcc matrix (d) FFT of region b (e) FFT of region c.

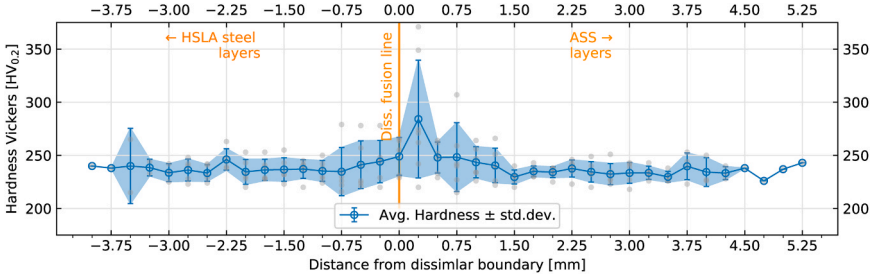

Fig. 3–14. Average and error measurement of Hardness Vickers measurements in the vicinity of the dissimilar fusion line. The vertical orange line at value 0 indicates the position of the interface relative to every indentation made. Positive values indicate measurements in the ASS layers. Negative values indicate measurements in the HSLA steel layers.

strength and subsequent specimen failure. The position of the kink is indicated by the red arrow in the inset of Fig. 3–15.a.

With the help of the DIC system, it is possible to identify the origin of the observed inflection point and sudden increase in stiffness. Fig. 3–15. c shows the strain distribution maps of the uniaxial engineering strain. At lower load levels the strain is distributed homogeneously all throughout. Further loading is accompanied by deformation in the vicinity of the fusion boundary of the first and second ASS layers and is shown as such at stress level of 464 MPa. Further on, shear deformation takes place within the first and second ASS layers, until both material

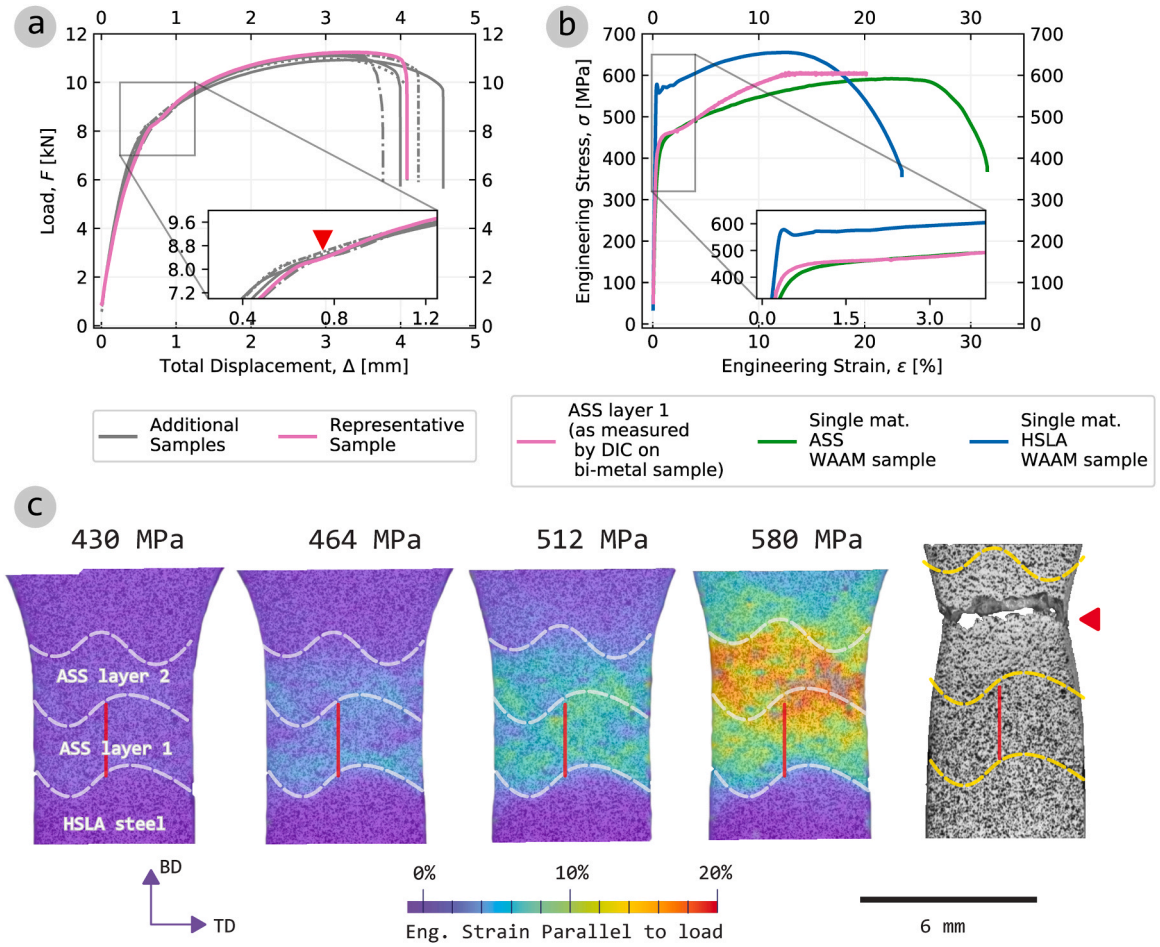

Fig. 3–15. (a) Load-Displacement curves of bi-metal tensile coupons, with inset showing position of inflection point as highlighted by the red marker. (b) Stress-strain curves for the interface layer (ASS layer 1) obtained from DIC measurements with a virtual gauge length such as the one shown in red in (c). Reference curves for mono-material specimens are included for ASS and HSLA steel. Strain distribution maps in (c) indicate engineering strain component in the direction of the tensile load. Approximate location of ASS layers 1 and 2 are delimited with dashed lines. Failure location is highlighted with a red marker.

volumes develop substantial plastic deformation. It is at this point, that differences start to appear between the layers of ASS. From 580 MPa onward, the strain distribution map shows a large cluster of highly deformed material at the second ASS layer, which continues to elongate down to necking and final failure.

It is through this strain distribution map that a reasonable relationship can be established between the microstructural and the mechanical properties of the diluted material. As the fusion boundary of the first diluted layer is partially populated by martensite, strain may be localized on the austenite matrix in its immediate vicinity. Moreover, the higher degree of ferrite content in the diluted ASS layer, as well as a higher density of high angle boundaries between crystals may help to constraint the development of plastic deformation in the diluted layer. The comparatively high volume of ferrite content may restrict the dislocation motion in the large austenite grains. Comparatively, the neighboring layer of ASS with almost nominal composition displays a low yield point and a large work-hardening behavior. This material volume shows also large columnar grains without the additional ferrite content. As tensile deformation progresses, most elongation is expressed as plastic deformation of the 2nd layer of ASS until final necking and breaking. At such point, the 1st ASS layer is also heavily deformed, showing local strains of above 20% relative elongation.

During the progression of the tensile test, however, the HSLA steel develops a very small amount of plastic deformation. This small plastic strain is understandable, as the ASS work-hardens up to the yield strength of the HSLA steel. Fig. 3–15b may help illustrate why plastic deformation is concentrated within the undiluted ASS layers. The yield point of the HSLA steel is close to, although lower than, the ultimate tensile strength of the ASS. This seems to be true even under diluted conditions. Nonetheless, the diluted interface layer shows higher yield point and a larger work-hardening behavior than the undiluted ASS. The difference in yield behavior of the interface layer compared to the HSLA steel and ASS benchmarks is highlighted on the inset of Fig. 3–15b.The summarized information on tensile behavior and deformation capacity is also available in tabulated form in Table 3–1.

4. Conclusions

Additive manufacturing establishes a path to produce functionally

Table 3–1
Yield strength, tensile strength, and elongation after fracture for bi-metal tensile specimens, as well as Austenitic Stainless Steel and High Strength Low Alloy Steel benchmark values. (*) Necking occurs outside of gauge length.

	Yield Strength σ_y [MPa]	Tensile Strength σ_u [MPa]	Elongation at fracture Δ/L_0 [%]
Bi-metal interface (ASS layer 1)	411 ± 11.9	592 ± 10.7	19.8 ± 4.9 (*)
ASS WAAM benchmark	392 ± 6.27	592 ± 23.8	29.7 ± 1.3
HSLA steel WAAM benchmark	576 ± 19.5	667 ± 19.5	24.5 ± 2.1

graded components. A clear challenge when attempting to do so is the mixing of dissimilar alloys, and the consequences therefrom. Throughout this work, functional grading of a High-Strength Low-Alloy (HSLA) steel with an Austenitic Stainless Steel (ASS) is carried out by manufacturing a bi-metal structure through wire arc additive manufacturing (WAAM). While there has been prior research on this material combination, it is yet to be adequately described the nature of the microstructure observed. A comprehensive analysis of the microstructure of this highly heterogeneous interface is essential to establish an adequate correlation with its observed functional performance. Thus, the work provides a detailed description of the microstructural features observed at the dissimilar interface layer. It does so in a holistic approach, including phase constitution, chemical composition, crystallography and complimented by thermomechanical modeling and characterization of its bulk mechanical properties. After in-depth characterization at macro-, micro- and nano- length scales of the interface between both alloys, the following conclusions are made:

- Macroscopic examination of the interface layer revealed the formation of ferritic bands alongside austenite. EPMA analysis detected chromium and nickel segregation, matching the spatial location of the ferritic bands.
- The Schaeffler diagram is useful to predict mixed ASS layer microstructure. However, the chosen deposition parameters yield heterogeneous mixtures in the melt pool, leading to chemical composition variations at the fusion boundary and within the weld metal.
- Bainitic ferrite coexists with martensite at the HSLA steel and first-deposited ASS fusion line. Crystallographic analysis shows a Bain-like orientation relationship in all ferrite phases with the surrounding austenite matrix. Parent Austenite Grain (PAG) reconstruction supports crystallographic alignment of primary austenite grains during solidification, confirming grain boundary migration and growth of the austenite phase across the fusion boundary.
- Beyond the fusion boundary, the interface layer contains stratified ferrite alongside an austenite matrix. Most ferrite within austenite grains have the same crystallographic orientation. Some ferritic islands exhibit bainitic features with an acicular morphology containing smaller parallel lath packages.
- Multi-bead depositions behave as a large heat sink during the solidification and cooling of the deposited material. Although solidification and cooling rates may be high in multi-bead deposits, and even more so when deposited using Cold-Metal Transfer, they are not high enough to form organized dislocation cell walls of segregated elemental composition in the ASS matrix, as those observed in laser-DED methods.
- Hardness indentations reveal the effect of islands within the first ASS layer up to 250 μm away from the fusion boundary. In these islands hardness may reach 371 $HV_{0.2}$, or about 50% higher than the surrounding material.
- Digital image correlation during tensile testing reveals a comparable quasi-static behavior of the first ASS interface layer with that behavior displayed by the neighboring ASS layers. For this first diluted layer, yield stress is estimated to be 411 MPa and tensile strength is estimated at 592 MPa. At lower stress levels, deformation concentrates in the region of the dissimilar fusion boundary, but further deformation localizes within the 2nd ASS layer all throughout necking and failure.

Through the extent of this work, a better link between the alloys chosen, the microstructure formed after deposition and the local mechanical properties is provided. The microstructural characterization presented is a necessary empirical study for the further prediction of the mechanical and functional performance of large-scale ASS-HSLA bi-metal components produced by additive manufacturing. For future work, mechanical properties, such as fatigue and fracture behavior, at and around the interface will be characterized and correlated with the microstructural features observed in this study.

CRediT authorship contribution statement

Galán Argumedo José Luis: Writing – review & editing, Writing – original draft, Visualization, Methodology, Investigation, Formal analysis, Data curation, Conceptualization. **Mahmoudiniya M.:** Writing – review & editing, Validation, Investigation. **Reinton T.E.:** Writing – review & editing, Validation, Investigation, Formal analysis. **Kestens L. A.I:** Writing – review & editing, Resources. **Hermans M.J.M:** Writing – review & editing, Supervision, Resources, Project administration, Funding acquisition, Conceptualization. **Popovich V.A.:** Writing – review & editing, Supervision, Resources, Project administration, Funding acquisition, Conceptualization.

Declaration of Competing Interest

The authors declare the following financial interests/personal relationships which may be considered as potential competing interests Marcel Hermans reports financial support was provided by European Commission.

Data Availability

The raw/processed data required to reproduce these findings cannot be shared at this time as the data also forms part of an ongoing study.

Acknowledgements

This research is supported by the Materials innovation institute M2i (www.m2i.nl). The authors acknowledge support regarding TEM results (F.D. Tichelaar, Kavli Institute of Nanoscience, Delft University of Technology), K. Kwakernaak and R. Hendrikx at the Department of Materials Science and Engineering of the Delft University of Technology is acknowledged for the EPMA and X-ray analysis.

References

"3Dprint AM 316L." Böhler Welding by Voestalpine, p. 2019, 2019, [Online]. Available: ⟨https://www.vabw-service.com/voestalpine/⟩.
"3Dprint AM 46." Böhler Welding by Voestalpine, p. 2018, 2018, [Online]. Available: ⟨https://www.vabw-service.com/voestalpine/⟩.
O.D. Acevedo, "Assessing Mechanical Performance of Dissimilar Steel Systems Made Via Wire-Arc Additive Manufacturing," University of Tennessee, 2021.
Ahsan, M.R.U., et al., 2020. Heat-treatment effects on a bimetallic additively-manufactured structure (BAMS) of the low-carbon steel and austenitic-stainless steel. Addit. Manuf. vol. 32 (October 2019), 101036 https://doi.org/10.1016/j.addma.2020.101036.
Ahsan, M.R.U., Tanvir, A.N.M., Ross, T., Elsawy, A., Oh, M.S., Kim, D.B., 2019. Fabrication of bimetallic additively manufactured structure (BAMS) of low carbon steel and 316L austenitic stainless steel with wire + arc additive manufacturing. Rapid Prototyp. J. vol. 26 (3), 519–530. https://doi.org/10.1108/RPJ-09-2018-0235.
F. Armao, L. Byall, and D. Koteckl, *Gas Metal Arc welding: Product and Procedure Selection*. Cleveland, OH: Lincoln Global Inc., 2014.
ASTM, 2017. ASTM E92-17 Standard Test Methods for Vickers Hardness and Knoop Hardness of Metallic Materials. ASTM International,, West Conshohocken, USA.
ASTM, 2020. *Standard Test Method for Determining Volume Fraction by Systematic Manual Point Count*. E562-19. ASTM International,.
AWS, 2005. AWS A5.18/A5.18M:2005 Specificaiton for Carbon Steel Electrodes and Rods for Gas Shielded Arc Welding. ANSI,, Miami, USA.
AWS, 2012. AWS A5.9/A5.9M:2012 Specification for Bare Stainless Steel Welding Electrodes and Rods. AWS A5.9/A5.9M:2012, American Welding Society,, Miami, USA.
Baek, M.S., Kim, K.S., Park, T.W., Ham, J., Lee, K.A., 2020. Quantitative phase analysis of martensite-bainite steel using EBSD and its microstructure, tensile and high-cycle fatigue behaviors. Mater. Sci. Eng. A vol. 785 (April). https://doi.org/10.1016/j.msea.2020.139375.
Bayerlein, M., Christ, H.J., Muchrabi, H., 1989. Plasticity-induced maretensitic transofrmation during cyclic deformaton of AISI304 stainless steel. Mater. Sci. Eng. vol. 114, L11–L16. https://doi.org/10.1016/0921-5093(89)90871-X.
Bertsch, K.M., Meric de Bellefon, G., Kuehl, B., Thoma, D.J., 2020. Origin of dislocation structures in an additively manufactured austenitic stainless steel 316L. Acta Mater. vol. 199, 19–33. https://doi.org/10.1016/j.actamat.2020.07.063.

Bhadeshia, H.K.D.H., 2006. Worked Examples in the Geometry of Crystals, 2nd ed..,. The Institute of Materials,, Brookfield, USA.
Blakey-Milner, B., et al., 2021. Metal additive manufacturing in aerospace: A review. Mater. Des. vol. 209, 110008 https://doi.org/10.1016/j.matdes.2021.110008.
DuPont, J.N., Kusko, C.S., 2007. Technical note: Martensite formation in austenitic/ferritic dissimilar alloy welds. Weld. J. (Miami, Fla) vol. 86 (2).
DuPont, J.N., Marder, A.R., 1995. Thermal efficiency of arc welding processes. Weld. J. (Miami, Fla) vol. 74 (12), 406-s.
Elmer, J.W., Allen, S.M., Eagar, T.W., 1989. Microstructural development during solidification of stainless steel alloys. Metall. Trans. A vol. 20 (10), 2117–2131. https://doi.org/10.1007/BF02650298.
Ermakova, A., Mehmanparast, A., Ganguly, S., Razavi, J., Berto, F., 2020. Investigation of mechanical and fracture properties of wire and arc additively manufactured low carbon steel components. Theor. Appl. Fract. Mech. vol. 109 (May), 102685 https://doi.org/10.1016/j.tafmec.2020.102685.
Githinji, D.N., Northover, S.M., Bouchard, P.J., Rist, M.A., 2013. An EBSD study of the deformation of service-aged 316 austenitic steel. Metall. Mater. Trans. A Phys. Metall. Mater. Sci. vol. 44 (9), 4150–4167. https://doi.org/10.1007/s11661-013-1787-7.
Hsieh, C.-C., Wu, W., 2012. Overview of Intermetallic Sigma (σ) Phase Precipitation in Stainless Steels. ISRN Met. vol. 2012 (4), 1–16. https://doi.org/10.5402/2012/732471.
Huang, C., Kyvelou, P., Zhang, R., Ben Britton, T., Gardner, L., 2022. Mechanical testing and microstructural analysis of wire arc additively manufactured steels. Mater. Des. vol. 216, 110544 https://doi.org/10.1016/j.matdes.2022.110544.
Inoue, H., Koseki, T., Ohkita, S., Fuji, M., 2000. Formation mechanism of vermicular and lacy ferrite in austenitic stainless steel weld metals. Sci. Technol. Weld. Join. vol. 5 (6), 385–396. https://doi.org/10.1179/136217100101538452.
ISO, 2015. ISO/TR 18491 Welding and Allied Processes - Guidelines for Measurement of Welding Energies. ISO,, Geneva.
Izadi, M., Farzaneh, A., Mohammed, M., Gibson, I., Rolfe, B., 2020. A review of laser engineered net shaping (LENS) build and process parameters of metallic parts. Rapid Prototyp. J. vol. 26 (6), 1059–1078. https://doi.org/10.1108/RPJ-04-2018-0088.
Kou, S., 2021. Macrosegregation in the Fusion Zone. Welding Metallurgy. John Wiley & Sons, In.,, Hoboken.
Kou, S., Yang, Y.K., 2007. Fusion-boundary macrosegregation in dissimilar-filler welds. Weld. J. (Miami, Fla) vol. 86 (10), 303–312.
Laghi, V., et al., 2021. Experimentally-validated orthotropic elastic model for Wire-and-Arc Additively Manufactured stainless steel. Addit. Manuf. vol. 42 (February), 101999 https://doi.org/10.1016/j.addma.2021.101999.
Lin, Z., et al., 2020. Deposition of Stellite 6 alloy on steel substrates using wire and arc additive manufacturing. Int. J. Adv. Manuf. Technol. vol. 111 (1–2), 411–426. https://doi.org/10.1007/s00170-020-06116-w.
Lippold, J.C., Kotecki, D.J., 2005. Welding Metallurgy and Weldability of Stainless Steels, 1st ed..,. John Wiley & Sons,.
Liu, L., et al., 2018. Dislocation network in additive manufactured steel breaks strength – ductility trade-off. Mater. Today vol. 21 (4), 354–361. https://doi.org/10.1016/j.mattod.2017.11.004.
Lu, J., et al., 2016. Stacking fault energies in austenitic staniless steels. Acta Metarialia vol. 111, 39–46. https://doi.org/10.1016/j.actamat.2016.03.042.
Mas, F., et al., 2016. Heterogeneities in local plastic flow behavior in a dissimilar weld between low-alloy steel and stainless steel. Mater. Sci. Eng. A vol. 667, 156–170. https://doi.org/10.1016/j.msea.2016.04.082.
Maurya, A.K., Pandey, C., Chhibber, R., 2023. Influence of heat input on weld integrity of weldments of two dissimilar steels. Mater. Manuf. Process. vol. 38 (4), 379–400. https://doi.org/10.1080/10426914.2022.2075889.
Mishra, A., Paul, A.R., Mukherjee, M., Kumar, R., Kumar Sharma, A., 2023. Evaluation of Cu-Ti dissimilar interface characteristics for wire arc additive manufacturing process. Rapid Prototyp. J. vol. 29 (2), 366–377. https://doi.org/10.1108/RPJ-05-2022-0142.
Nelson, T.W., Lippold, J.C., Mills, M.J., 1998. Investigation of boundaries and structures in dissimilar metal welds. Sci. Technol. Weld. Join. vol. 3 (5), 249–255. https://doi.org/10.1179/stw.1998.3.5.249.
Nelson, T.W., Lippold, J.C., Mills, M.J., 1999. Nature and evolution of the fusion boundary in ferritic-austenitic dissimilar weld metals, Part 1 - nucleation and growth. Weld. J. (Miami, Fla) vol. 78 (10), 329-s.
NEN-ISO, *EN-ISO 6892–1:2019 Metallic materials - Tensile Testing - Part 1: Method of test at room temperature*, no. december 2019. Belgium, 2019.
Ornath, F., Soudry, J., Weiss, B.Z., Minkoff, I., 1981. Weld Pool Segregation During the Welding of Low Alloy Steels With Austenitic Electrodes. Weld. J. (Miami, Fla) vol. 60 (11), 1227–1230.
Padilha, A.F., Escriba, D.M., Materna-Morris, E., Rieth, M., Klimenkov, M., 2007. Precipitation in AISI 316L(N) during creep tests at 550 and 600 °C up to 10 years. J. Nucl. Mater. vol. 362 (1), 132–138. https://doi.org/10.1016/j.jnucmat.2006.12.027.
Pichler, P., Simonds, B.J., Sowards, J.W., 2020. Measurements of thermophysical properties of solid and liquid NIST SRM 316L stainless steel. J. Mater. Sci. vol. 55 (9), 4081–4093. https://doi.org/10.1007/s10853-019-04261-6.
Rani, K.U., et al., 2022. Wire Arc Additive Manufactured Mild Steel and Austenitic Stainless Steel Components: Microstructure, Mechanical Properties and Residual Stresses. Mater. (Basel) vol. 15 (20). https://doi.org/10.3390/ma15207094.
Raut, L.P., Taiwade, R.V., 2021. Wire arc additive manufacturing: a comprehensive review and research directions. J. Mater. Eng. Perform. vol. 30 (7), 4768–4791. https://doi.org/10.1007/s11665-021-05871-5.
Rees, G.I., H.K.D.H, B., 1994. Thermodynamics of acicular ferrite nucleation. Mater. Sci. Technol. vol. 10 (5), 353–358.
Savage, W.F., Nippes, E.F., Szekeres, E.S., 1976. Study of Weld Interface Phenomena in a Low Alloy Steel. Weld. J. (Miami, Fla) vol. 55 (9).
J.A. Self, D.L. Olson, and G.R. Edwards, "The stability of austenitic weld metal," 1984.
Shrestha, S.L., Breen, A.J., Trimby, P., Proust, G., Ringer, S.P., Cairney, J.M., 2014. An automated method of quantifying ferrite microstructures using electron backscatter diffraction (EBSD) data. Ultramicroscopy vol. 137, 40–47. https://doi.org/10.1016/j.ultramic.2013.11.003.
Soderstrom, E.E., Scott, K.M., Mendez, P.F., 2011. Calorimetric Measurement of Droplet Temperature in GMAW. Weld. J. vol. 90 (4), 77–84.
Sourmail, T., 2001. Precipitation in creep resistant austenitic stainless steels. Mater. Sci. Technol. vol. 17 (1), 1–14. https://doi.org/10.1179/026708301101508972.
Sridar, S., Sargent, N., Wang, X., Klecka, M.A., Xiong, W., 2022. Determination of Location-Specific Solidification Cracking Susceptibility for a Mixed Dissimilar Alloy Processed by Wire-Arc Additive Manufacturing. Met. (Basel) vol. 12 (284). https://doi.org/10.3390/met12020284.
Sun, C., Wang, Y., McMurtrey, M.D., Jerred, N.D., Liou, F., Li, J., 2021. Additive manufacturing for energy: A review. Appl. Energy vol. 282 (September 2020). https://doi.org/10.1016/j.apenergy.2020.116041.
Thome, P., Schneider, M., Yardley, V.A., Payton, E.J., Eggeler, G., 2022. Crystallographic Analysis of Plate and Lath Martensite in Fe-Ni Alloys. Crystals vol. 12 (2), 11–13. https://doi.org/10.3390/cryst12020156.
Wang, C., Liu, T.G., Zhu, P., Lu, Y.H., Shoji, T., 2020. Study on microstructure and tensile properties of 316L stainless steel fabricated by CMT wire and arc additive manufacturing. Mater. Sci. Eng. A vol. 796 (June). https://doi.org/10.1016/j.msea.2020.140006.
Wang, S., Chen, C., Ju, J., Zhou, J., Xue, F., 2023. Suppression of LME cracks in Sn bronze-steel system based on multi-material additive manufacturing. Mater. Lett. vol. 335 (December 2022), 133775 https://doi.org/10.1016/j.matlet.2022.133775.
Zhang, Q., et al., 2020. Predictions of solute mixing in a weld pool and macrosegregation formation during dissimilar-filler welding of aluminum alloys: Modeling and experiments. J. Mater. Res. Technol. vol. 9 (6), 12080–12090. https://doi.org/10.1016/j.jmrt.2020.08.109.